Available online at www.sciencedirect.com
ScienceDirect
Comput. Methods Appl. Mech. Engrg. 414 (2023) 116180
Computer methods in applied mechanics and engineering
www.elsevier.com/locate/cma

Phase-field modeling and consistent energy-stable simulation of binary creeping flows in contact with solid

Junxiang Yang[a], Jingwen Wu[a], Zhijun Tan[a,b,*]

[a] School of Computer Science and Engineering, Sun Yat-sen University, Guangzhou 510006, China
[b] Guangdong Province Key Laboratory of Computational Science, Sun Yat-sen University, Guangzhou 510275, China

Received 23 February 2023; received in revised form 24 May 2023; accepted 6 June 2023
Available online xxxx

Abstract

In this work, we present an efficient and practical model for describing two-phase creeping fluid flows in contact with a solid substrate. In the framework of phase-field method, a ternary Cahn–Hilliard model is modified by adding a term reflecting the wetting condition of liquid phase on the liquid–solid interface. The contact angle dynamics can be implicitly achieved by solving the phase-field equations and the explicit treatment on liquid–solid boundary is absent. Therefore, various discretization methods in space can be naturally adopted. To update the creeping flows in arbitrary domains, we herein consider the incompressible Darcy equations with a penalty term. The coupled binary fluid system theoretically satisfies the energy dissipation law with respect to a total energy functional. An energy dissipation-preserving time-marching scheme is constructed based on the auxiliary variable approach. Furthermore, a simple correction technique is utilized to improve the consistency between original and numerical values. We analytically prove that the proposed scheme still satisfies the energy law in its discrete version. Extensive numerical experiments are performed to validate the accuracy, consistent stability, and capability of our method.

Keywords: Binary creeping flows; Phase-field model; Irregular domains; Energy-stable algorithm

1. Introduction

The creeping flow extensively exists in micro-tube, porous medium, and Hele–Shaw cell [1,2]. The incompressible Darcy model is effective to describe the dynamics of creeping flow. During the past few years, the numerical algorithms and simulations of Darcy-type fluid flows have been investigated in [3–5] and references therein. However, most of these researches treated the computational domain as a regular cube and did not consider the effect of solid obstacles on the dynamics of fluid interface.

When it comes to the binary fluids in contact with solid, two fundamental questions arise: (i) how to accurately describe the fluid interface ? (ii) how to efficiently treat the wetting boundary condition on the fluid–solid interface ? The phase-field method [6–8] is a popular approach to answer the first question because the changes of fluid interface can be implicitly captured by solving the phase-field equations. The Cahn–Hilliard (CH) equation is a well-known phase-field model in fluid field because it has a good property of mass conservation. For the numerical methods of

* Corresponding author at: School of Computer Science and Engineering, Sun Yat-sen University, Guangzhou 510006, China.
E-mail addresses: yangjx79@mail.sysu.edu.cn (J. Yang), tzhij@mail.sysu.edu.cn (Z. Tan).

https://doi.org/10.1016/j.cma.2023.116180
0045-7825/

CH model, please refer to [9–14]. For the industrial applications of CH equation, see [15–18] and references therein. To answer the second question, the finite element method [19] is practical to treat the irregular boundary. In the present work, we focus on proposing a new approach to capture the fluid interface and reflect the wetting condition in a totally implicit manner. Moreover, we hope that our proposed model is not limited to a specific discretization method in space. In [20,21], authors observed that the evolution of a particular fluid component in space can be suppressed by the existences of other immiscible components. For a three-component fluid system, the interfaces are governed by [22–25]

$$\xi \frac{\partial \phi_i}{\partial t} = \frac{1}{Pe} \Delta \mu_i, \tag{1.1}$$

$$\mu_i = F'(\phi_i) + \beta(\boldsymbol{\phi}) - \epsilon^2 \Delta \phi_i, \quad i = 0, 1, 2, \tag{1.2}$$

where $\phi_i = \phi_i(\mathbf{x}, t)$ represents the concentration of ith fluid component, $\mathbf{x}$ and t are spatial and temporal variables. We let $\phi_i \approx 1$ and 0 in the interior and exterior of ith fluid, respectively. The chemical potential of ith fluid is μ_i. The Peclet number is $Pe = U_c L_c/(M\mu_c) > 0$, where U_c is the characteristic velocity, L_c is the characteristic length, M is the mobility, μ_c is the characteristic chemical potential. The thickness of diffuse interface is reflected by a small positive constant ϵ, $\xi > 0$ is a constant. For a Darcy fluid system, ξ represents the porosity. The nonlinear term is $F'(\phi_i) = \phi_i^3 - \phi_i$. The Lagrange multiplier $\beta(\boldsymbol{\phi})$ is used to satisfy the link condition, i.e., $\phi_0 + \phi_1 + \phi_2 = 1$ [22–25].

The present work aims to develop a practical and efficient phase-field model to implicitly describe the wetting condition of binary creeping fluids in contact with solid. The irregular domain occupied by fluid phases is embedded in a large regular domain (full domain). On the boundary of regular domain, the simple boundary conditions (periodic or homogeneous-Neumann) are considered. With the absence of explicit treatment of wetting boundary condition on fluid–solid interface, our proposed model naturally describes the wetting phenomenon by solving the governing equations. Therefore, the proposed model is efficient to implement and various methods for the discretization in space can be theoretically adopted. Furthermore, the proposed fluid system consisting of phase-field model and Darcy model can lead to an energy dissipation law. Based on this property, we design a linear and energy-stable scheme based on the scalar auxiliary variable (SAV) type method [26–28]. As reported in [29,30], the original SAV method cannot satisfy the consistency between original and numerical variables when a larger time step is used. To fix this problem, we adopt two correction techniques and analytically demonstrate the corrected energy dissipation law in time-discretized version. The present method not only achieves simple computation of wetting phenomenon on fluid–solid interface but also preserves the energy property of a dissipative system.

The rests of this article are as follows. In Section 2, the governing equations of binary creeping fluids in contact with solid are derived. The consistent energy-stable algorithm and the numerical implementation are introduced in Section 3. In Section 4, the numerical experiments are performed to validate the proposed method. The concluding remarks are given in Section 5.

2. Phase-field model in contact with solid

For the immiscible fluid system, the multi-component CH model [22–25] can prevent the permeation of bulk phases from different fluid materials. By utilizing this property, we consider a ternary CH model (Eqs. (1.1) and (1.2)) and fix one component all along in the computation, i.e., we only solve the rest two fluid components. The fixed component ϕ_0 is regarded as the solid obstacle or the arbitrary domain. In the interior and exterior of solid, we assume $\phi_0 = 1$ and $\phi_0 = 0$, respectively. In each position of the system, we still require the conservative condition, i.e., $\phi_0 + \phi_1 + \phi_2 = 1$. To derive a phase-field model reflecting the wetting condition, we start from the following Young's equality which describes the relationship between fluid–solid contact angle and interfacial tensions

$$\sigma_{12} \cos\theta = \sigma_{2S} - \sigma_{1S}, \tag{2.1}$$

where σ_{12}, σ_{2S}, and σ_{1S} are the surface tensions on the interfaces of liquid 1 and liquid 2, liquid 2 and solid, liquid 1 and solid, respectively. The contact angle is θ, see Fig. 1 for the schematic illustration.

On the interface of liquid and solid, the following equality holds

$$\nabla \phi_m \cdot \mathbf{n}_S = -|\nabla \phi_m| \cos\theta_m, \quad m = 1, 2, \tag{2.2}$$

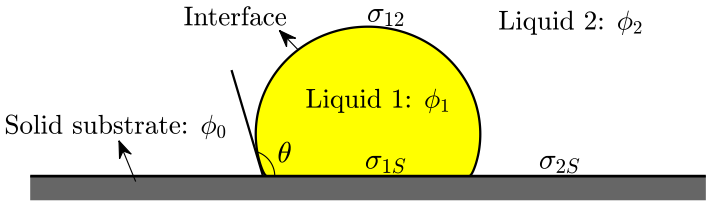

Fig. 1. Schematic illustration of a droplet locating on the solid. Here, the contact angle is θ.

where $\mathbf{n}_S = \nabla\phi_0/|\nabla\phi_0|$ is the unit normal vector to solid, $\theta_1 = 180^\circ - \theta$, and $\theta_2 = 180^\circ - \theta_1$. For the CH-type phase-field model, the local equilibrium approximation of diffuse interface leads to $|\nabla\phi_m| = \phi_m(1-\phi_m)/(\sqrt{2}\epsilon)$ [22,23]. Thus, we rewrite Eq. (2.2) as

$$\epsilon^2\nabla\phi_0\cdot\nabla\phi_m + \epsilon\phi_m(1-\phi_m)|\nabla\phi_0|\cos\theta_m/\sqrt{2} = 0. \tag{2.3}$$

Theoretically, we can use Eq. (2.2) to construct the model without the aforementioned local equilibrium approximation. In this work, we want to avoid numerically calculating $|\nabla\phi_m|$. Moreover, the polynomial form is helpful to derive an energy structure in Theorem 2.1. Since the right-hand side of Eq. (2.3) is zero, we claim the terms on left-hand side are "zero-contribution". By adding them into the expression of μ_m (i.e., Eq. (1.2)), the following equation is obtained

$$\mu_m = f(\phi_m) + \beta(\boldsymbol{\phi}) + \frac{\epsilon}{\sqrt{2}}\phi_m(1-\phi_m)|\nabla\phi_0|\cos\theta_m - \epsilon^2\nabla\cdot((1-\phi_0)\nabla\phi_m) - \epsilon^2\phi_0\Delta\phi_m, \tag{2.4}$$

where we use $\Delta\phi_m = \nabla\cdot((1-\phi_0)\nabla\phi_m) + \nabla\phi_0\cdot\nabla\phi_m + \phi_0\Delta\phi_m$. In the regions occupied by liquid, $\phi_0 = 0$ indicates Eq. (2.4) is equivalent to the original expression of μ_m (i.e., Eq. (1.2)). In the diffuse interface, the last term in Eq. (2.4) indeed exists. However, the diffuse interface becomes narrow as the refinement of mesh size. Furthermore, we notice that this term does not have contributions to mass conservation and wetting condition (i.e., it does not contain contact angle θ). As $\phi_0 \to 0$, the last term in Eq. (2.4) also vanishes. For convenience, we neglect the last term and recast Eq. (2.4) as

$$\mu_m = f(\phi_m) + \beta(\boldsymbol{\phi}) + \frac{\epsilon}{\sqrt{2}}\phi_m(1-\phi_m)|\nabla\phi_0|\cos\theta_m - \epsilon^2\nabla\cdot((1-\phi_0)\nabla\phi_m). \tag{2.5}$$

To suppress the evolution of ϕ_m in solid, we rewrite $\Delta\mu_m$ as $\nabla\cdot((1-\phi_0)\nabla\mu_m)$. The modified phase-field equations read as

$$\xi\frac{\partial\phi_m}{\partial t} = \frac{1}{Pe}\nabla\cdot((1-\phi_0)\nabla\mu_m), \tag{2.6}$$

$$\mu_m = f(\phi_m) + \beta(\boldsymbol{\phi}) + \frac{\epsilon}{\sqrt{2}}\phi_m(1-\phi_m)|\nabla\phi_0|\cos\theta_m - \epsilon^2\nabla\cdot((1-\phi_0)\nabla\phi_m), \quad m = 1, 2. \tag{2.7}$$

In this model, the solid is embedded into a regular full domain Ω. The profile of solid is defined by the 0.5 level-set of the initial value of ϕ_0. On the boundary of Ω (i.e., $\partial\Omega$), the periodic or the homogeneous Neumann (i.e., $\nabla\phi_m\cdot\mathbf{n} = 0$ and $\nabla\mu_m\cdot\mathbf{n} = 0$) boundary condition is used, $\mathbf{n}$ is the outward unit normal vector to the domain boundary. To satisfy $\phi_0 + \phi_1 + \phi_2 = 1$, we derive a specific form of $\beta(\boldsymbol{\phi})$. By summing Eq. (2.6) from $m = 0$ to 2, we get

$$\sum_{m=0}^{2}\frac{1}{Pe}\nabla\cdot((1-\phi_0)\nabla\mu_m) = \xi\frac{\partial(\sum_{m=0}^{2}\phi_m)}{\partial t} = 0. \tag{2.8}$$

Because $1-\phi_0$ is generally not equal to zero everywhere, we simply set $\sum_{m=0}^{2}\mu_m = 0$ to suppress the time evolution of $\sum_{m=0}^{2}\phi_m$. Since $\frac{\partial\phi_0}{\partial t} = 0$, we can define the form of μ_0 in an arbitrary manner. Here, we let

$$\mu_0 = f(\phi_0) + \beta(\boldsymbol{\phi}) - \epsilon^2\nabla\cdot((1-\phi_0)\nabla\phi_0). \tag{2.9}$$

By summing Eq. (2.7) for $m = 1$ and 2 and combining it with Eq. (2.9), we have

$$\sum_{m=0}^{2}f(\phi_m) + 3\beta(\boldsymbol{\phi}) + \sum_{m=1}^{2}\left[\frac{\epsilon}{\sqrt{2}}\phi_m(1-\phi_m)|\nabla\phi_0|\cos\theta_m\right] - \epsilon^2\nabla\cdot\left[(1-\phi_0)\nabla\left(\sum_{m=0}^{2}\phi_m\right)\right] = \sum_{m=0}^{2}\mu_m = 0.$$

Because $\nabla\left(\sum_{m=0}^{2}\phi_m\right)=\nabla 1=0$, we derive a specific Lagrange multiplier as follows:

$$\beta(\boldsymbol{\phi})=-\frac{1}{3}\left[\sum_{m=1}^{2}\left(f(\phi_m)+\frac{\epsilon}{\sqrt{2}}\phi_m(1-\phi_m)|\nabla\phi_0|\cos\theta_m\right)+f(\phi_0)\right]. \tag{2.10}$$

To describe the evolution of velocity field in a domain with solid obstacles, Bergmann et al. [31] treated the whole region as a porous medium and introduced a penalty term into the incompressible Navier–Stokes equations to suppress the evolution of velocities in solid. Their framework is efficient to implement because the calculation can be naturally performed on Cartesian grids. Based on the similar idea, we propose a modified version of incompressible Darcy model as

$$\frac{ReDa}{\xi}\frac{\partial\mathbf{u}}{\partial t}+\alpha(\boldsymbol{\phi})\mathbf{u}=-\nabla p-\frac{\epsilon^{-1}}{We}\sum_{m=1}^{2}\phi_m\nabla\mu_m+\frac{\phi_0}{\kappa}(\mathbf{u}_S-\mathbf{u}), \tag{2.11}$$

$$\nabla\cdot\mathbf{u}=0. \tag{2.12}$$

where $\mathbf{u}=(u,v)$ or (u,v,w) is the velocity field in two-dimensional (2D) or three-dimensional (3D) space, p is the pressure. The non-dimensional numbers are Reynolds number $Re=\rho_c U_c L_c/\nu_c$, Darcy number $Da=\xi_c/L_c^2$, Weber number $We=\rho_c L_c U_c^2/\sigma$, where ρ_c is the characteristic density, ν_c is the characteristic viscosity, ξ_c is the characteristic permeability, σ is the surface tension coefficient. Some details can refer to [32,33]. $\alpha(\boldsymbol{\phi})=\eta(\boldsymbol{\phi})/\chi$ is the hydraulic conductivity, $\eta(\boldsymbol{\phi})=\eta_1\phi_1+\eta_2\phi_2$, η_m is the viscosity of mth liquid, $\chi>0$ is a constant permeability. The last term in Eq. (2.11) plays an effect of penalty and $0<\kappa\ll 1$ is a constant. The velocity of solid is $\mathbf{u}_S$. In the present work, we only consider the fixed solid and Eqs. (2.11) and (2.12) can be simplified as

$$\frac{ReDa}{\xi}\frac{\partial\mathbf{u}}{\partial t}+\alpha(\boldsymbol{\phi})\mathbf{u}=-\nabla p-\frac{\epsilon^{-1}}{We}\sum_{m=1}^{2}\phi_m\nabla\mu_m-\frac{\phi_0}{\kappa}\mathbf{u}, \tag{2.13}$$

$$\nabla\cdot\mathbf{u}=0. \tag{2.14}$$

By adding the convection term into the modified phase-field model and considering Eqs. (2.13) and (2.14), the creeping flow-coupled two-phase model with wetting condition in contact with solid reads as

$$\xi\frac{\partial\phi_m}{\partial t}+\nabla\cdot(\mathbf{u}\phi_m)=\frac{1}{Pe}\nabla\cdot((1-\phi_0)\nabla\mu_m), \tag{2.15}$$

$$\mu_m=f(\phi_m)+\beta(\boldsymbol{\phi})+\frac{\epsilon}{\sqrt{2}}\phi_m(1-\phi_m)|\nabla\phi_0|\cos\theta_m-\epsilon^2\nabla\cdot((1-\phi_0)\nabla\phi_m),\quad m=1,2. \tag{2.16}$$

$$\frac{ReDa}{\xi}\frac{\partial\mathbf{u}}{\partial t}+\alpha(\boldsymbol{\phi})\mathbf{u}=-\nabla p-\frac{\epsilon^{-1}}{We}\sum_{m=1}^{2}\phi_m\nabla\mu_m-\frac{\phi_0}{\kappa}\mathbf{u}, \tag{2.17}$$

$$\nabla\cdot\mathbf{u}=0. \tag{2.18}$$

On $\partial\Omega$, the velocities are periodic or satisfy $\mathbf{u}|_{\partial\Omega}=0$. To facilitate the readers to understand the following contents, we first define some useful notations. Let F_1 and F_2 be two functions, the L^2-inner product and the L^2-norm are defined as $(F_1,F_2)=\int_\Omega F_1\cdot F_2\,d\mathbf{x}$ and $\|F_1\|^2=(F_1,F_1)$, respectively.

Theorem 2.1. *With appropriate boundary conditions (i.e., periodic or homogeneous-Neumann for scalar variables, and $\mathbf{u}|_{\partial\Omega}=0$), Eqs. (2.15)–(2.18) satisfy an energy dissipation law with respect to the following energy functional*

$$E(\boldsymbol{\phi},\mathbf{u})=\frac{\xi\epsilon^{-1}}{We}\sum_{m=1}^{2}\left[\int_\Omega F(\phi_m)\,d\mathbf{x}+\int_\Omega\epsilon\left(\frac{\phi_m^2}{2}-\frac{\phi_m^3}{3}\right)|\nabla\phi_0|\cos\theta_m\,d\mathbf{x}+\int_\Omega\frac{\epsilon^2}{2}(1-\phi_0)|\nabla\phi_m|^2\,d\mathbf{x}\right]$$
$$+\frac{ReDa}{2\xi}\int_\Omega|\mathbf{u}|^2\,d\mathbf{x}. \tag{2.19}$$

Proof. By taking the L^2-inner product of Eq. (2.15) with μ_m, we have

$$\xi\left(\frac{\partial\phi_m}{\partial t},\mu_m\right)+(\nabla\cdot(\mathbf{u}\phi_m),\mu_m)=-\frac{1}{Pe}\|\sqrt{1-\phi_0}\nabla\mu_m\|^2. \tag{2.20}$$

By taking the L^2-inner product of Eq. (2.16) with $\frac{\partial \phi_m}{\partial t}$, we have

$$\left(\mu_m, \frac{\partial \phi_m}{\partial t}\right) = \frac{d}{dt}\int_\Omega F(\phi_m)\, d\mathbf{x} + \left(\beta(\boldsymbol{\phi}), \frac{\partial \phi_m}{\partial t}\right) + \frac{d}{dt}\int_\Omega \epsilon\left(\frac{\phi_m^2}{2} - \frac{\phi_m^3}{3}\right)|\nabla\phi_0|\cos\theta_m\, d\mathbf{x} \tag{2.21}$$

$$+ \frac{d}{dt}\int_\Omega \frac{\epsilon^2}{2}(1-\phi_0)|\nabla\phi_m|^2\, d\mathbf{x}. \tag{2.22}$$

By multiplying Eq. (2.17) with $\mathbf{u}$ and taking the inner product, we get

$$\frac{ReDa}{2\xi}\frac{d}{dt}\int_\Omega |\mathbf{u}|^2\, d\mathbf{x} + \int_\Omega \alpha(\boldsymbol{\phi})|\mathbf{u}|^2\, d\mathbf{x} = -\frac{\epsilon^{-1}}{We}\left(\sum_{m=1}^{2}\phi_m\nabla\mu_m, \mathbf{u}\right) - \int_\Omega \frac{\phi_0}{\kappa}|\mathbf{u}|^2\, d\mathbf{x}. \tag{2.23}$$

From $m = 1$ to 2, we multiply Eq. (2.20) with $\frac{\epsilon^{-1}}{We}$, Eq. (2.22) with $\frac{\xi\epsilon^{-1}}{We}$, and combine the results with Eq. (2.23), the following inequality is derived

$$\frac{\xi\epsilon^{-1}}{We}\sum_{m=1}^{2}\left[\frac{d}{dt}\int_\Omega F(\phi_m)\, d\mathbf{x} + \frac{d}{dt}\int_\Omega \epsilon\left(\frac{\phi_m^2}{2} - \frac{\phi_m^3}{3}\right)|\nabla\phi_0|\cos\theta_m\, d\mathbf{x} + \frac{d}{dt}\int_\Omega \frac{\epsilon^2}{2}(1-\phi_0)|\nabla\phi_m|^2\, d\mathbf{x}\right]$$

$$+ \frac{ReDa}{2\xi}\frac{d}{dt}\int_\Omega |\mathbf{u}|^2\, d\mathbf{x} = -\int_\Omega \alpha(\boldsymbol{\phi})|\mathbf{u}|^2\, d\mathbf{x} - \frac{\epsilon^{-1}}{WePe}\sum_{m=1}^{2}\|\sqrt{1-\phi_0}\nabla\mu_m\|^2 - \int_\Omega \frac{\phi_0}{\kappa}|\mathbf{u}|^2\, d\mathbf{x} \le 0. \tag{2.24}$$

It is worth noting that the integration-by-parts, divergence theory, and appropriate boundary conditions are used in the estimation. The aforementioned inequality completes the proof. □

Remark 2.1. To justify the motivation and facilitate the interested readers, we first perform a literature survey on typical ternary phase-field models and then present the reasons for choosing the adopted model. By considering the interfacial tensions on three fluid interfaces and the interaction between different components, Boyer and Lapuerta [34] originally developed a coupled nonlinear ternary CH model. Based on their model, the totally and partially spreading states of fluids can be simulated by changing the surface tension coefficients. Recently, Zhang and Yang [35] utilized the SAV method to design a linear, second-order time-accurate, and energy-stable scheme for solving Boyer's model. Huang [36] adopted Boyer's model and the hybrid immersed boundary lattice Boltzmann method to simulate the incompressible ternary droplets on irregular solids. It is worth noting that Boyer's model is not trivial for N-component fluid systems ($N > 3$) because the surface tension coefficients are not uniquely determined, see the discussions in [37]. To fix this problem, Kim [22] presented a simple ternary phase-field model by naturally combining the free energy functionals of binary system. In Kim's model, the phase-field variables were only used to capture the fluid interfaces. The interfacial tensions were reflected by some generalized surface tension formulations [37,38] in momentum equation. Since this approach avoided introducing the relation of surface tension coefficients in model, it can be extended into an arbitrary N-component fluid system. Moreover, the admissible of this model belongs to a Gibbs triangle. Based on Kim's ternary model, Park and Anderson [39] simulated the double emulsion formation in a T-junction. Mu et al. [40] performed simulations of coaxial liquid jets in a co-flow focusing device. Howard et al. [41] adopted a similar idea to construct a conservative multi-component level-set method for N-phase flows. Inspired by Kim's multi-phase model, Xia et al. [42] recently developed an N-component L^2 phase field fluid model. In the present work, one component is fixed as a solid and the interactions between fluid and solid are implicitly reflected by some penalty terms. Because Kim's model (Eqs. (1.1) and (1.2)) not only satisfies the structure of a Gibbs triangle but also naturally becomes a binary model in fluid regions, we can efficiently construct the desired model after some modifications. Moreover, this model has good potential to investigate arbitrary N-components fluids in complex domains.

Remark 2.2. For a ternary CH system, the Lagrange multiplier prevents the penetration of different fluid components in bulk phases. This treatment has a similar effect with the well-known diffuse-domain (DD) method [43,44] in constructing complex domains. Compared with the DD method, the present model not only analytically satisfies the mass conservation of each fluid component (i.e., $\frac{d}{dt}\int_\Omega \phi_m\, d\mathbf{x} = 0$) but also leads to an energy dissipation law. Although the phase-field approximation leads to a finite diffusion at fluid–solid interface, this phenomenon can be reduced by refining the mesh size. The grid convergence tests in Section 4 will clarify this.

Remark 2.3. Let m_1 and m_2 be the masses of fluid 1 and 2 in a binary CH fluid system, the order parameter can be defined as $\phi = (m_1 - m_2)/(m_1 + m_2)$ or $m_1/(m_1 + m_2)$ [6]. The first definition makes $\phi \in [-1, 1]$, the second definition represents the fraction of concentration and makes $\phi \in [0, 1]$. These definitions only reflect different scaling effects and both of them have been extensively used in previous works [45–47]. For a ternary system, many researchers [22–25] used $\phi_m \in [0, 1]$ $m = 1, 2, 3$ because the constraint $\phi_1 + \phi_2 + \phi_3 = 1$ should be satisfied. It is worth noting that the proposed model is a modified version of ternary CH system, we also consider $\phi_m \in [0, 1]$ in this work.

3. Numerical method and energy estimation

It is worth noting that the direct discretization scheme of Eqs. (2.15)–(2.18) in time is hard to satisfy the unconditional energy stability. The SAV method [48,49] is practical to construct linear and energy-stable time-marching scheme for the complex phase-field fluid system. To utilize the SAV method, we first need to present the equivalent forms of Eqs. (2.15)–(2.18) in Section 3.1. Based on the equivalent model, a linear, temporally second-order accurate scheme is designed in Section 3.2. We analytically estimate the discrete version of energy dissipation law in Section 3.3. In Section 3.4, the implementation in one time step is introduced. For the spatial discretization, the numerical methods are not limited, i.e., we can use the finite difference method, the finite volume method, and the finite element method, etc.

3.1. Equivalent model

Based on the similar idea of SAV approach [48,49], we define the time-dependent auxiliary variables as

$$R = R(t) = \sqrt{\int_\Omega \sum_{m=1}^{2} \left[F(\phi_m) + \frac{\epsilon}{\sqrt{2}} \left(\frac{\phi_m^2}{2} - \frac{\phi_m^3}{3} \right) |\nabla \phi_0| \cos\theta_m \right] d\mathbf{x} + C},$$

$$Q = Q(t) = 1, \quad \frac{dQ}{dt} = 0.$$

Here, $C > 0$ is a constant to ensure the value beneath the square root be positive. In SAV method, we note that the definitions of auxiliary variables R and Q only are mathematical techniques which facilitate us to derive the equivalent equations and design the energy dissipation-preserving scheme. By utilizing these variables, we recast Eqs. (2.15)–(2.18) to be the following equivalent equations

$$\xi \frac{\partial \phi_m}{\partial t} + Q \nabla \cdot (\mathbf{u} \phi_m) = \frac{1}{Pe} \nabla \cdot ((1 - \phi_0) \nabla \mu_m), \tag{3.1}$$

$$\mu_m = R(H_m + \tilde{\beta}(\boldsymbol{\phi})) - \epsilon^2 \nabla \cdot ((1 - \phi_0) \nabla \phi_m), \tag{3.2}$$

$$\frac{ReDa}{\xi} \frac{\partial \mathbf{u}}{\partial t} + \alpha(\boldsymbol{\phi}) \mathbf{u} = -\nabla p - \frac{Q \epsilon^{-1}}{We} \sum_{m=1}^{2} \phi_m \nabla \mu_m - \frac{\phi_0}{\kappa} \mathbf{u}, \tag{3.3}$$

$$\nabla \cdot \mathbf{u} = 0, \tag{3.4}$$

$$\frac{dR}{dt} = \frac{1}{2} \int_\Omega \sum_{m=1}^{2} H_m \frac{\partial \phi_m}{\partial t} \, d\mathbf{x}, \tag{3.5}$$

$$\frac{dQ}{dt} = \int_\Omega \sum_{m=1}^{2} [\nabla \cdot (\mathbf{u} \phi_m) + \phi_m \nabla \mu_m \cdot \mathbf{u}] \, d\mathbf{x}. \tag{3.6}$$

It is worth noting that Eqs. (3.5) and (3.6) provide the evolutional equations for R and Q, respectively. Eq. (3.6) holds because $\int_\Omega [\nabla \cdot (\mathbf{u} \phi_m) + \phi_m \nabla \mu_m \cdot \mathbf{u}] \, d\mathbf{x} = 0$ for $m = 1, 2$. Here, we have

$$H_m = \frac{f(\phi_m) + \frac{\epsilon}{\sqrt{2}} \phi_m (1 - \phi_m) |\nabla \phi_0| \cos\theta_m}{\sqrt{\int_\Omega \sum_{m=1}^{2} \left[F(\phi_m) + \frac{\epsilon}{\sqrt{2}} \left(\frac{\phi_m^2}{2} - \frac{\phi_m^3}{3} \right) |\nabla \phi_0| \cos\theta_m \right] d\mathbf{x} + C}},$$

$$\tilde{\beta}(\boldsymbol{\phi}) = -\frac{1}{3}\left[\sum_{m=1}^{2} H_m + \frac{f(\phi_0)}{\sqrt{\int_\Omega \sum_{m=1}^{2}\left[F(\phi_m) + \frac{\epsilon}{\sqrt{2}}\left(\frac{\phi_m^2}{2} - \frac{\phi_m^3}{3}\right)|\nabla\phi_0|\cos\theta_m\right] d\mathbf{x} + C}}\right].$$

Since Eqs. (3.5) and (3.6) are ordinary differential equations with respect to time, we do not need to define extra boundary conditions for R and Q.

3.2. Numerical scheme

Let $(\cdot)^n$ be the approximation at nth time level, our proposed scheme consists of steps 1–3 in one time step.

Step 1. With computed values at previous time steps, we update ϕ_m^{n+1}, μ_m^{n+1}, $\mathbf{u}^{n+1}$, p^{n+1}, $\hat{R}^{n+1}$, and $\hat{Q}^{n+1}$ from the following second-order backward difference formula (BDF2)

$$\xi\left(\frac{3\phi_m^{n+1} - 4\phi_m^n + \phi_m^{n-1}}{2\Delta t}\right) + \hat{Q}^{n+1}\nabla\cdot(\mathbf{u}^*\phi_m^*) = \frac{1}{Pe}\nabla\cdot((1-\phi_0)\nabla\mu_m^{n+1}), \tag{3.7}$$

$$\mu_m^{n+1} = \hat{R}^{n+1}(H_m^* + \tilde{\beta}(\boldsymbol{\phi}^*)) - \epsilon^2\nabla\cdot((1-\phi_0)\nabla\phi_m^{n+1}) + S(\phi_m^{n+1} - \phi_m^*), \tag{3.8}$$

$$\frac{ReDa}{\xi}\left(\frac{3\tilde{\mathbf{u}}^{n+1} - 4\mathbf{u}^n + \mathbf{u}^{n-1}}{2\Delta t}\right) + \alpha(\boldsymbol{\phi}^*)\tilde{\mathbf{u}}^{n+1} = -\nabla p^n - \frac{\hat{Q}^{n+1}\epsilon^{-1}}{We}\sum_{m=1}^{2}\phi_m^*\nabla\mu_m^* - \frac{\phi_0}{\kappa}\tilde{\mathbf{u}}^{n+1}, \tag{3.9}$$

$$\frac{ReDa}{\xi}\left(\frac{3\mathbf{u}^{n+1} - 3\tilde{\mathbf{u}}^{n+1}}{2\Delta t}\right) = -\left(\nabla p^{n+1} - \nabla p^n\right), \tag{3.10}$$

$$\nabla\cdot\mathbf{u}^{n+1} = 0, \tag{3.11}$$

$$3\hat{R}^{n+1} - 4R^n + R^{n-1} = \frac{1}{2}\int_\Omega \sum_{m=1}^{2} H_m^*\cdot\left(3\phi_m^{n+1} - 4\phi_m^n + \phi_m^{n-1}\right) d\mathbf{x}, \tag{3.12}$$

$$\frac{3\hat{Q}^{n+1} - 4Q^n + Q^{n-1}}{2\Delta t} = \int_\Omega \sum_{m=1}^{2}\left[\nabla\cdot(\mathbf{u}^*\phi_m^*)\mu_m^{n+1} + \phi_m^*\nabla\mu_m^*\cdot\tilde{\mathbf{u}}^{n+1}\right] d\mathbf{x}. \tag{3.13}$$

Here, the periodic boundary condition or the following boundary conditions are considered

$$\mathbf{u}^{n+1}\cdot\mathbf{n}|_{\partial\Omega} = 0,\ \tilde{\mathbf{u}}^{n+1}|_{\partial\Omega} = 0,\ \nabla\phi_m^{n+1}\cdot\mathbf{n}|_{\partial\Omega} = 0,$$
$$\nabla\mu_m^{n+1}\cdot\mathbf{n}|_{\partial\Omega} = 0,\ \nabla p^{n+1}\cdot\mathbf{n}|_{\partial\Omega} = \nabla p^n\cdot\mathbf{n}|_{\partial\Omega}.$$

The last term in Eq. (3.8) plays a role of stabilization, $S > 0$ is a stabilization parameter. As reported in [29], the SAV-based time-marching scheme leads to the inconsistency between the original energy (i.e., Eq. (2.19)) and the modified energy obtained by the solutions of the aforementioned equations. To improve the consistency, the following energy correction technique is used after step 1.

Step 2. $R^{n+1} = \gamma_o\hat{R}^{n+1} + (1-\gamma_o)J(\boldsymbol{\phi})$, where

$$J(\boldsymbol{\phi}) = \sqrt{\int_\Omega \sum_{m=1}^{2}\left[F(\phi_m) + \frac{\epsilon}{\sqrt{2}}\left(\frac{\phi_m^2}{2} - \frac{\phi_m^3}{3}\right)|\nabla\phi_0|\cos\theta_m\right] d\mathbf{x} + C}.$$

Here, $\gamma_o = \min\gamma$ and $\gamma \in [0, 1]$ such that

$$\frac{1}{2}\left(|R^{n+1}|^2 + |2R^{n+1} - R^n|^2\right) - \frac{1}{2}\left(|\hat{R}^{n+1}|^2 + |2\hat{R}^{n+1} - R^n|^2\right) \le \Delta t q_1 \sum_{m=1}^{2}\|\sqrt{1-\phi_0}\nabla\mu_m^{n+1}\|^2, \tag{3.14}$$

where $0 < q_1 \le \frac{1}{Pe\xi}$, the aforementioned inequality can be simplified to be

$$a\gamma^2 + b\gamma + c \le 0, \tag{3.15}$$

where

$$a = \frac{5}{2}\left(\hat{R}^{n+1} - J(\boldsymbol{\phi})\right)^2,\ b = \left(\hat{R}^{n+1} - J(\boldsymbol{\phi}^{n+1})\right)\left(5J(\boldsymbol{\phi}^{n+1}) - 2R^n\right),$$

$$c = \frac{1}{2}\left(|J(\boldsymbol{\phi}^{n+1})|^2 + |2J(\boldsymbol{\phi}^{n+1} - R^n)|^2 - |\hat{R}^{n+1}|^2 - |2\hat{R}^{n+1} - R^n|^2\right) - \Delta t q_1 \sum_{m=1}^{2} \|\sqrt{1-\phi_0}\nabla\mu_m^{n+1}\|^2.$$

It is worth noting that $a+b+c \le 0$ when $a \neq 0$, then we have $\gamma_o = \max\{0, (-b - \sqrt{b^2-4ac})/2a\}$. If $a = 0$, the correction is not needed.

Besides the energy correction in step 2, it is also important to correct the numerical value of Q because it will deviate away from the exact value 1 with the increase of time step. The numerical results in Section 4 verify this. This inconsistency makes the numerical solution does not correspond to the original Darcy model. To fix this, the following correction step is needed after steps 1 and 2.

Step 3. $Q^{n+1} = \nu_o \hat{Q}^{n+1} + (1-\nu_o)$. Here, $\nu_o = \min \nu$ and $\nu \in [0,1]$ such that

$$\frac{1}{2}\left(|Q^{n+1}|^2 + |2Q^{n+1} - Q^n|^2\right) - \frac{1}{2}\left(|\hat{Q}^{n+1}|^2 + |2\hat{Q}^{n+1} - Q^n|^2\right) \le \Delta t q_2 \|\sqrt{\phi_0}\tilde{\mathbf{u}}^{n+1}\|^2, \tag{3.16}$$

where $0 < q_2 \le \frac{2We}{\kappa\epsilon^{-1}}$. We can simplify the aforementioned inequality as

$$c\nu^2 + e\nu + f \le 0, \tag{3.17}$$

where

$$d = 5\left(\hat{Q}^{n+1} - 1\right)^2, \quad e = 4\left(Q^n - 1\right)\left(1 - \hat{Q}^{n+1}\right),$$
$$f = 5 - |Q^n|^2 - 4Q^n - \Delta t q_2 \|\sqrt{\phi_0}\tilde{\mathbf{u}}^{n+1}\|^2.$$

We notice that $d+e+f \le 0$ when $d \neq 0$ and we have $\nu_o = \max\{0, (-e - \sqrt{e^2-4df})/2d\}$. If $d = 0$, we do not perform the correction.

3.3. Discrete energy dissipation law

In this subsection, we estimate the discrete version of energy dissipation law. By taking the L^2-inner product of Eq. (3.7) with $\frac{2\Delta t\epsilon^{-1}}{We}\mu_m^{n+1}$, we get

$$\frac{\xi\epsilon^{-1}}{We}\left(3\phi_m^{n+1} - 4\phi_m^n + \phi_m^{n-1}, \mu_m^{n+1}\right) + \frac{2\Delta t\epsilon^{-1}\hat{Q}^{n+1}}{We}\left(\nabla\cdot(\mathbf{u}^*\phi_m^*), \mu_m^{n+1}\right)$$
$$= -\frac{2\Delta t\epsilon^{-1}}{WePe}\|\sqrt{1-\phi_0}\nabla\mu_m^{n+1}\|^2. \tag{3.18}$$

By taking the L^2-inner product of Eq. (3.8) with $\frac{\xi\epsilon^{-1}}{We}(3\phi_m^{n+1} - 4\phi_m^n + \phi_m^{n-1})$, we get

$$\frac{\xi\epsilon^{-1}}{We}\left(\mu_m^{n+1}, 3\phi_m^{n+1} - 4\phi_m^n + \phi_m^{n-1}\right) = \frac{\xi\epsilon^{-1}\hat{Q}^{n+1}}{We}\left(H_m^*, 3\phi_m^{n+1} - 4\phi_m^n + \phi_m^{n-1}\right)$$
$$+ \frac{\xi\epsilon^{-1}\hat{Q}^{n+1}}{We}\left(\tilde{\beta}(\boldsymbol{\phi}), 3\phi_m^{n+1} - 4\phi_m^n + \phi_m^{n-1}\right) + \frac{\xi\epsilon}{2We}\left(\|\sqrt{1-\phi_0}\nabla\phi_m^{n+1}\|^2 + \|\sqrt{1-\phi_0}(2\nabla\phi_m^{n+1} - \nabla\phi_m^n)\|^2\right)$$
$$- \frac{\xi\epsilon}{2We}\left(\|\sqrt{1-\phi_0}\nabla\phi_m^n\|^2 + \|\sqrt{1-\phi_0}(2\nabla\phi_m^n - \nabla\phi_m^{n-1})\|^2\right) + \frac{\xi\epsilon}{2We}\|\sqrt{1-\phi_0}(\nabla\phi_m^{n+1} - 2\nabla\phi_m^n + \nabla\phi_m^{n-1})\|^2$$
$$+ \frac{S\xi\epsilon^{-1}}{We}\|\phi_m^{n+1} - \phi_m^n\|^2 - \frac{S\xi\epsilon^{-1}}{We}\|\phi_m^n - \phi_m^{n-1}\|^2 + \frac{2S\xi\epsilon^{-1}}{We}\|\phi_m^{n+1} - 2\phi_m^n + \phi_m^{n-1}\|^2. \tag{3.19}$$

By multiplying Eq. (3.12) with $\frac{2\xi\epsilon^{-1}}{We}\hat{Q}^{n+1}$, we have

$$\frac{\xi\epsilon^{-1}}{We}\left(|\hat{Q}^{n+1}|^2 + |2\hat{Q}^{n+1} - Q^n|^2\right) - \frac{\xi\epsilon^{-1}}{We}\left(|Q^n|^2 + |2Q^n - Q^{n-1}|^2\right)$$
$$+ \frac{\xi\epsilon^{-1}}{We}|\hat{Q}^{n+1} - 2Q^n + Q^{n-1}|^2 = \frac{\xi\epsilon^{-1}}{We}\left(\hat{Q}^{n+1}\sum_{m=1}^{2} H_m^*, 3\phi_m^{n+1} - 4\phi_m^n + \phi_m^{n-1}\right). \tag{3.20}$$

By combining Eqs. (3.18)–(3.20) for $m = 1$ to 2, we get

$$\begin{aligned}
&\frac{\xi\epsilon^{-1}}{We}\left(|\hat{R}^{n+1}|^2+|2\hat{R}^{n+1}-R^n|^2\right)-\frac{\xi\epsilon^{-1}}{We}\left(|R^n|^2+|2R^n-R^{n-1}|^2\right)+\frac{\xi\epsilon}{2We}\sum_{m=1}^{2}\Big(\|\sqrt{1-\phi_0}\nabla\phi_m^{n+1}\|^2\\
&+\|\sqrt{1-\phi_0}(2\nabla\phi_m^{n+1}-\nabla\phi_m^n)\|^2\Big)-\frac{\xi\epsilon}{2We}\sum_{m=1}^{2}\Big(\|\sqrt{1-\phi_0}\nabla\phi_m^n\|^2+\|\sqrt{1-\phi_0}(2\nabla\phi_m^n-\nabla\phi_m^{n-1})\|^2\Big)\\
&+\frac{S\xi\epsilon^{-1}}{We}\sum_{m=1}^{2}\|\phi_m^{n+1}-\phi_m^n\|^2-\frac{S\xi\epsilon^{-1}}{We}\sum_{m=1}^{2}\|\phi_m^n-\phi_m^{n-1}\|^2+\sum_{m=1}^{2}\frac{2\Delta t\,\hat{Q}^{n+1}\epsilon^{-1}}{We}\left(\nabla\cdot(\mathbf{u}^*\phi_m^*),\mu_m^{n+1}\right)\\
&+\frac{\xi\epsilon^{-1}\hat{Q}^{n+1}}{We}\underbrace{\left(\tilde{\beta}(\boldsymbol{\phi}),\sum_{m=1}^{2}(3\phi_m^{n+1}-4\phi_m^n+\phi_m^{n-1})\right)}_{\mathrm{I}}=-\frac{2\Delta t\epsilon^{-1}}{WePe}\sum_{m=1}^{2}\|\sqrt{1-\phi_0}\nabla\mu_m^{n+1}\|^2\\
&-\frac{\xi\epsilon}{2We}\sum_{m=1}^{2}\|\sqrt{1-\phi_0}(\nabla\phi_m^{n+1}-2\nabla\phi_m^n+\nabla\phi_m^{n-1})\|^2-\frac{2S\xi\epsilon^{-1}}{We}\sum_{m=1}^{2}\|\phi_m^{n+1}-2\phi_m^n+\phi_m^{n-1}\|^2\\
&-\frac{\xi\epsilon^{-1}}{We}|\hat{R}^{n+1}-2R^n+R^{n-1}|^2.
\end{aligned}\tag{3.21}$$

Because of $\phi_0+\phi_1+\phi_2=1$, term I becomes $(\tilde{\beta}(\boldsymbol{\phi}),3(1-\phi_0)-4(1-\phi_0)+(1-\phi_0))=0$. By taking the L^2-inner product of Eq. (3.9) with $2\Delta t\tilde{\mathbf{u}}^{n+1}$, we have

$$\begin{aligned}
\frac{ReDa}{\xi}\left(3\tilde{\mathbf{u}}^{n+1}-4\mathbf{u}^n+\mathbf{u}^{n-1},\tilde{\mathbf{u}}^{n+1}\right)+2\Delta t\|\sqrt{\alpha(\boldsymbol{\phi}^*)}\tilde{\mathbf{u}}^{n+1}\|^2&=2\Delta t\left(-\nabla p^n,\tilde{\mathbf{u}}^{n+1}\right)-\frac{2\Delta t}{\kappa}\|\sqrt{\phi_0}\tilde{\mathbf{u}}^{n+1}\|^2\\
&-\frac{2\Delta t\,\hat{Q}^{n+1}\epsilon^{-1}}{We}\left(\sum_{m=1}^{2}\phi_m^*\nabla\mu_m^*,\tilde{\mathbf{u}}^{n+1}\right),
\end{aligned}\tag{3.22}$$

where

$$\begin{aligned}
&\left(3\tilde{\mathbf{u}}^{n+1}-4\mathbf{u}^n+\mathbf{u}^{n-1},\tilde{\mathbf{u}}^{n+1}\right)=\frac{1}{2}\left(\|\mathbf{u}^{n+1}\|^2-\|\mathbf{u}^n\|^2+\|2\mathbf{u}^{n+1}-\mathbf{u}^n\|^2-\|2\mathbf{u}^n-\mathbf{u}^{n-1}\|^2\right.\\
&\left.+\|\mathbf{u}^{n+1}-2\mathbf{u}^n+\mathbf{u}^{n-1}\|^2\right)+3\left(\|\tilde{\mathbf{u}}^{n+1}\|^2-\|\mathbf{u}^{n+1}\|^2\right).
\end{aligned}$$

By squaring Eq. (3.10), we have

$$\left(\nabla p^n,\tilde{\mathbf{u}}^{n+1}\right)=\frac{3ReDa}{4\xi\Delta t}\left(\|\mathbf{u}^{n+1}\|^2-\|\tilde{\mathbf{u}}^{n+1}\|^2\right)+\frac{\xi\Delta t}{3ReDa}\left(\|\nabla p^{n+1}\|^2-\|\nabla p^n\|^2\right).\tag{3.23}$$

By taking the inner product of Eq. (3.10) with $2\Delta t\mathbf{u}^{n+1}$, we get

$$\frac{3}{2}\|\tilde{\mathbf{u}}^{n+1}\|^2-\frac{3}{2}\|\mathbf{u}^{n+1}\|^2=\frac{3}{2}\|\mathbf{u}^{n+1}-\tilde{\mathbf{u}}^{n+1}\|^2.\tag{3.24}$$

Putting Eqs. (3.22) and (3.23) together, we get

$$\begin{aligned}
&\frac{ReDa}{2\xi}\left(\|\mathbf{u}^{n+1}\|^2-\|\mathbf{u}^n\|^2+\|2\mathbf{u}^{n+1}-\mathbf{u}^n\|^2-\|2\mathbf{u}^n-\mathbf{u}^{n-1}\|^2+\|\mathbf{u}^{n+1}-2\mathbf{u}^n+\mathbf{u}^{n-1}\|^2\right)\\
&+\frac{3ReDa}{\xi}\left(\|\mathbf{u}^{n+1}\|^2-\|\mathbf{u}^{n+1}\|^2\right)+2\Delta t\|\sqrt{\alpha(\boldsymbol{\phi}^*)}\tilde{\mathbf{u}}^{n+1}\|^2=-\frac{3ReDa}{2\xi}\left(\|\mathbf{u}^{n+1}\|^2-\|\tilde{\mathbf{u}}^{n+1}\|^2\right)\\
&-\frac{2\xi\Delta t^2}{3ReDa}\left(\|\nabla p^{n+1}\|^2-\|\nabla p^n\|^2\right)-\frac{2\Delta t\,\hat{Q}^{n+1}\epsilon^{-1}}{We}\left(\sum_{m=1}^{2}\phi_m^*\nabla\mu_m^*,\tilde{\mathbf{u}}^{n+1}\right)-\frac{2\Delta t}{\kappa}\|\sqrt{\phi_0}\tilde{\mathbf{u}}^{n+1}\|^2.
\end{aligned}\tag{3.25}$$

By multiplying Eq. (3.24) with $\frac{ReDa}{\xi}$ and combining with Eq. (3.25), we have

$$\begin{aligned}
&\frac{ReDa}{2\xi}\left(\|\mathbf{u}^{n+1}\|^2+\|2\mathbf{u}^{n+1}-\mathbf{u}^n\|^2-\|\mathbf{u}^n\|^2-\|2\mathbf{u}^n-\mathbf{u}^{n-1}\|^2\right)+\frac{2\xi\Delta t^2}{3ReDa}\left(\|\nabla p^{n+1}\|^2-\|\nabla p^n\|^2\right)\\
&=-\frac{ReDa}{2\xi}\|\mathbf{u}^{n+1}-2\mathbf{u}^n+\mathbf{u}^{n-1}\|^2-2\Delta t\|\sqrt{\alpha(\boldsymbol{\phi}^*)}\tilde{\mathbf{u}}^{n+1}\|^2-\frac{3ReDa}{2\xi}\|\mathbf{u}^{n+1}-\tilde{\mathbf{u}}^{n+1}\|^2-\frac{2\Delta t}{\kappa}\|\sqrt{\phi_0}\tilde{\mathbf{u}}^{n+1}\|^2\\
&\quad-\frac{2\Delta t\hat{Q}^{n+1}\epsilon^{-1}}{We}\left(\sum_{m=1}^{2}\phi_m^*\nabla\mu_m^*,\tilde{\mathbf{u}}^{n+1}\right).
\end{aligned}\tag{3.26}$$

By multiplying Eq. (3.13) with $\hat{Q}^{n+1}$, we obtain

$$\begin{aligned}
&\frac{1}{2}\left(|\hat{Q}^{n+1}|^2-|Q^n|^2+|2\hat{Q}^{n+1}-Q^n|^2-|2Q^n-Q^{n-1}|^2\right)+\frac{1}{2}|\hat{Q}^{n+1}-2Q^n+Q^{n-1}|^2\\
&=2\Delta t\hat{Q}^{n+1}\sum_{m=1}^{2}\left[(\nabla\cdot(\mathbf{u}^*\phi_m^*),\mu_m^{n+1})+(\phi_m^*\nabla\mu_m^*,\tilde{\mathbf{u}}^{n+1})\right].
\end{aligned}\tag{3.27}$$

By multiplying Eq. (3.27) with $\frac{\epsilon^{-1}}{We}$ and combining with Eq. (3.26), we get

$$\begin{aligned}
&\frac{\epsilon^{-1}}{2We}\left(|\hat{Q}^{n+1}|^2+|2\hat{Q}^{n+1}-Q^n|^2-|Q^n|^2-|2Q^n-Q^{n-1}|^2\right)+\frac{ReDa}{2\xi}\left(\|\mathbf{u}^{n+1}\|^2+\|2\mathbf{u}^{n+1}-\mathbf{u}^n\|^2-\|\mathbf{u}^n\|^2\right.\\
&\left.-\|2\mathbf{u}^n-\mathbf{u}^{n-1}\|^2\right)+\frac{2\xi\Delta t^2}{3ReDa}\left(\|\nabla p^{n+1}\|^2-\|\nabla p^n\|^2\right)=-\frac{ReDa}{2\xi}\|\mathbf{u}^{n+1}-2\mathbf{u}^n+\mathbf{u}^{n-1}\|^2\\
&-2\Delta t\|\sqrt{\alpha(\boldsymbol{\phi}^*)}\tilde{\mathbf{u}}^{n+1}\|^2-\frac{3ReDa}{2\xi}\|\mathbf{u}^{n+1}-\tilde{\mathbf{u}}^{n+1}\|^2-\frac{2\Delta t}{\kappa}\|\sqrt{\phi_0}\tilde{\mathbf{u}}^{n+1}\|^2\\
&-\frac{\epsilon^{-1}}{2We}|\hat{Q}^{n+1}-2Q^n+Q^{n-1}|^2+\frac{2\Delta t\hat{Q}^{n+1}\epsilon^{-1}}{We}\sum_{m=1}^{2}\left(\nabla\cdot(\mathbf{u}^*\phi_m^*),\mu_m^{n+1}\right).
\end{aligned}\tag{3.28}$$

By multiplying Eq. (3.21) with $\frac{1}{2}$, Eq. (3.14) with $\frac{\xi\epsilon^{-1}}{We}$, and combing the results together, we have

$$\begin{aligned}
&\frac{\xi\epsilon^{-1}}{2We}\left(|R^{n+1}|^2+|2R^{n+1}-R^n|^2\right)-\frac{\xi\epsilon^{-1}}{2We}\left(|R^n|^2+|2R^n-R^{n-1}|^2\right)+\frac{\xi\epsilon}{4We}\sum_{m=1}^{2}\left(\|\sqrt{1-\phi_0}\nabla\phi_m^{n+1}\|^2\right.\\
&\left.+\|\sqrt{1-\phi_0}(2\nabla\phi_m^{n+1}-\nabla\phi_m^n)\|^2\right)-\frac{\xi\epsilon}{2We}\sum_{m=1}^{2}\left(\|\sqrt{1-\phi_0}\nabla\phi_m^n\|^2+\|\sqrt{1-\phi_0}(2\nabla\phi_m^n-\nabla\phi_m^{n-1})\|^2\right)\\
&+\frac{S\xi\epsilon^{-1}}{2We}\sum_{m=1}^{2}\|\phi_m^{n+1}-\phi_m^n\|^2-\frac{S\xi\epsilon^{-1}}{2We}\sum_{m=1}^{2}\|\phi_m^n-\phi_m^{n-1}\|^2+\frac{\Delta t\hat{Q}^{n+1}\epsilon^{-1}}{We}\sum_{m=1}^{2}\left(\nabla\cdot(\mathbf{u}^*\phi_m^*),\mu_m^{n+1}\right)=\\
&-\frac{\Delta t\epsilon^{-1}}{WePe}\sum_{m=1}^{2}\|\sqrt{1-\phi_0}\nabla\mu_m^{n+1}\|^2+\frac{q_1\Delta t\xi\epsilon^{-1}}{We}\sum_{m=1}^{2}\|\sqrt{1-\phi_0}\nabla\mu_m^{n+1}\|^2\\
&-\frac{\xi\epsilon}{4We}\sum_{m=1}^{2}\|\sqrt{1-\phi_0}(\nabla\phi_m^{n+1}-2\nabla\phi_m^n+\nabla\phi_m^{n-1})\|^2-\frac{S\xi\epsilon^{-1}}{We}\sum_{m=1}^{2}\|\phi_m^{n+1}-2\phi_m^n+\phi_m^{n-1}\|^2\\
&-\frac{\xi\epsilon^{-1}}{2We}|\hat{R}^{n+1}-2R^n+R^{n-1}|^2.
\end{aligned}\tag{3.29}$$

By multiplying Eq. (3.16) with $\frac{\epsilon^{-1}}{We}$ and combining the result with Eq. (3.28), we have

$$\begin{aligned}
&\frac{\epsilon^{-1}}{2We}\left(|Q^{n+1}|^2+|2Q^{n+1}-Q^n|^2-|Q^n|^2-|2Q^n-Q^{n-1}|^2\right)+\frac{2\xi\Delta t^2}{3ReDa}\left(\|\nabla p^{n+1}\|^2-\|\nabla p^n\|^2\right)\\
&+\frac{ReDa}{2\xi}\left(\|\mathbf{u}^{n+1}\|^2+\|2\mathbf{u}^{n+1}-\mathbf{u}^n\|^2-\|\mathbf{u}^n\|^2-\|2\mathbf{u}^n-\mathbf{u}^{n-1}\|^2\right)
\end{aligned}$$

$$= -\frac{ReDa}{2\xi}\|\mathbf{u}^{n+1} - 2\mathbf{u}^{n} + \mathbf{u}^{n-1}\|^2 - 2\Delta t\|\sqrt{\alpha(\boldsymbol{\phi})}\tilde{\mathbf{u}}^{n+1}\|^2 - \frac{3ReDa}{2\xi}\|\mathbf{u}^{n+1} - \tilde{\mathbf{u}}^{n+1}\|^2$$
$$+ \left(-\frac{2\Delta t}{\kappa} + \frac{q_2\Delta t\epsilon^{-1}}{We}\right)\|\sqrt{\phi_0}\tilde{\mathbf{u}}^{n+1}\|^2 - \frac{\epsilon^{-1}}{2We}|\hat{Q}^{n+1} - 2Q^{n} + Q^{n-1}|^2$$
$$+ \frac{2\Delta t\hat{Q}^{n+1}\epsilon^{-1}}{We}\sum_{m=1}^{2}\left(\nabla\cdot(\mathbf{u}^{*}\phi_m^{*}), \mu_m^{n+1}\right). \tag{3.30}$$

By multiplying Eq. (3.30) with $\frac{1}{2}$ and combining with Eq. (3.29), the desired energy dissipation law holds with respect to the following corrected energy functional

$$\frac{\xi\epsilon^{-1}}{2We}\left(|R^{n+1}|^2 + |2R^{n+1} - R^{n}|^2\right) + \frac{\xi\epsilon}{4We}\sum_{m=1}^{2}\left(\|\sqrt{1-\phi_0}\nabla\phi_m^{n+1}\|^2 + \|\sqrt{1-\phi_0}(2\nabla\phi_m^{n+1} - \nabla\phi_m^{n})\|^2\right)$$
$$+ \frac{S\xi\epsilon^{-1}}{2We}\sum_{m=1}^{2}\|\phi_m^{n+1} - \phi_m^{n}\|^2 + \frac{\epsilon^{-1}}{4We}\left(|Q^{n+1}|^2 + |2Q^{n+1} - Q^{n}|^2\right) + \frac{\xi\Delta t^2}{3ReDa}\|\nabla p^{n+1}\|^2$$
$$+ \frac{ReDa}{4\xi}\left(\|\mathbf{u}^{n+1}\|^2 + \|2\mathbf{u}^{n+1} - \mathbf{u}^{n}\|^2\right). \tag{3.31}$$

If we do not perform the corrections (i.e., step 2 and step 3), the resulting energy law corresponds to the following modified energy functional

$$\frac{\xi\epsilon^{-1}}{2We}\left(|\hat{R}^{n+1}|^2 + |2\hat{R}^{n+1} - R^{n}|^2\right) + \frac{\xi\epsilon}{4We}\sum_{m=1}^{2}\left(\|\sqrt{1-\phi_0}\nabla\phi_m^{n+1}\|^2 + \|\sqrt{1-\phi_0}(2\nabla\phi_m^{n+1} - \nabla\phi_m^{n})\|^2\right)$$
$$+ \frac{S\xi\epsilon^{-1}}{2We}\sum_{m=1}^{2}\|\phi_m^{n+1} - \phi_m^{n}\|^2 + \frac{\epsilon^{-1}}{4We}\left(|\hat{Q}^{n+1}|^2 + |2\hat{Q}^{n+1} - Q^{n}|^2\right) + \frac{\xi\Delta t^2}{3ReDa}\|\nabla p^{n+1}\|^2$$
$$+ \frac{ReDa}{4\xi}\left(\|\mathbf{u}^{n+1}\|^2 + \|2\mathbf{u}^{n+1} - \mathbf{u}^{n}\|^2\right). \tag{3.32}$$

In Section 4, the numerical examples will show that the correction techniques lead to highly consistent results.

Remark 3.1. Comparing with the traditional SAV method [48,49] in treating fluid equation, the proposed method introduces a correction technique to improve the consistence between the auxiliary variable Q and its exact value 1. The traditional SAV method cannot satisfy this consistency, then the computed solution is probably inaccurate if Q deviates away from 1. A numerical test in Section 4 will indicate that the proposed method leads to high consistency.

3.4. Numerical implementation

In step 1, it can be observed that the local variables (i.e., ϕ_m^{n+1}, μ_m^{n+1}, $\tilde{\mathbf{u}}^{n+1}$) and non-local variables (i.e., $\hat{R}^{n+1}$ and $\hat{Q}^{n+1}$) are coupled together. In this subsection, we introduce a splitting strategy to achieve totally decoupled computations. We let

$$\phi_m^{n+1} = \phi_{m,1}^{n+1} + \hat{Q}^{n+1}\phi_{m,2}^{n+1},\ \ \mu_m^{n+1} = \mu_{m,1}^{n+1} + \hat{Q}^{n+1}\mu_{m,2}^{n+1},$$
$$\hat{R}^{n+1} = \hat{R}_1^{n+1} + \hat{Q}^{n+1}\hat{R}_2^{n+1},\ \ \tilde{\mathbf{u}}^{n+1} = \tilde{\mathbf{u}}_1^{n+1} + \hat{Q}^{n+1}\tilde{\mathbf{u}}_2^{n+1}.$$

With the aforementioned expressions, we recast Eqs. (3.7) and (3.8) to be

$$\xi\frac{3(\phi_{m,1}^{n+1} + \hat{Q}^{n+1}\phi_{m,2}^{n+1}) - 4\phi_m^{n} + \phi_m^{n-1}}{2\Delta t} + \hat{Q}^{n+1}\nabla\cdot(\mathbf{u}^{*}\phi_m^{*}) = \frac{1}{Pe}\nabla\cdot((1-\phi_0)(\nabla\mu_{m,1}^{n+1}$$
$$+ \hat{Q}^{n+1}\nabla\mu_{m,2}^{n+1})), \tag{3.33}$$
$$\mu_{m,1}^{n+1} + \hat{Q}^{n+1}\mu_{m,2}^{n+1} = \hat{R}^{n+1}\left(H_m^{*} + \tilde{\beta}(\boldsymbol{\phi}^{*})\right) - \epsilon^2\nabla\cdot((1-\phi_0)(\nabla\phi_{m,1}^{n+1} + \hat{Q}^{n+1}\nabla\phi_{m,2}^{n+1}))$$
$$+ S(\phi_{m,1}^{n+1} + \hat{Q}^{n+1}\phi_{m,2}^{n+1} - \phi_m^{*}). \tag{3.34}$$

They can be split to be

$$\xi\frac{3\phi_{m,1}^{n+1}-4\phi_m^n+\phi_m^{n-1}}{2\Delta t}=\frac{1}{Pe}\nabla\cdot((1-\phi_0)\nabla\mu_{m,1}^{n+1}), \tag{3.35}$$

$$\mu_{m,1}^{n+1}=\hat{R}_1^{n+1}(H_m^*+\tilde{\beta}(\boldsymbol{\phi}^*))-\epsilon^2\nabla\cdot((1-\phi_0)\nabla\phi_{m,1}^{n+1})+S(\phi_{m,1}^{n+1}-\phi_m^*). \tag{3.36}$$

and

$$\xi\frac{3\phi_{m,2}^{n+1}}{2\Delta t}+\nabla\cdot(\mathbf{u}^*\phi_m^*)=\frac{1}{Pe}\nabla\cdot((1-\phi_0)\nabla\mu_{m,2}^{n+1}), \tag{3.37}$$

$$\mu_{m,2}^{n+1}=\hat{R}_2^{n+1}(H_m^*+\tilde{\beta}(\boldsymbol{\phi}^*))-\epsilon^2\nabla\cdot((1-\phi_0)\nabla\phi_{m,2}^{n+1}). \tag{3.38}$$

Let

$$\phi_{m,1}^{n+1}=\phi_{m,11}^{n+1}+\hat{R}_1^{n+1}\phi_{m,12}^{n+1},\ \mu_{m,1}^{n+1}=\mu_{m,11}^{n+1}+\hat{R}_1^{n+1}\mu_{m,12}^{n+1},$$
$$\phi_{m,2}^{n+1}=\phi_{m,21}^{n+1}+\hat{R}_2^{n+1}\phi_{m,22}^{n+1},\ \mu_{m,2}^{n+1}=\mu_{m,21}^{n+1}+\hat{R}_2^{n+1}\mu_{m,22}^{n+1}.$$

Using these expressions, we split Eqs. (3.35) and (3.36) to be

$$\xi\frac{3\phi_{m,11}^{n+1}-4\phi_m^n+\phi_m^{n-1}}{2\Delta t}=\frac{1}{Pe}\nabla\cdot((1-\phi_0)\nabla\mu_{m,11}^{n+1}), \tag{3.39}$$

$$\mu_{m,11}^{n+1}=-\epsilon^2\nabla\cdot((1-\phi_0)\nabla\phi_{m,11}^{n+1})+S(\phi_{m,11}^{n+1}-\phi_m^*), \tag{3.40}$$

and

$$\xi\frac{3\phi_{m,12}^{n+1}}{2\Delta t}=\frac{1}{Pe}\nabla\cdot((1-\phi_0)\nabla\mu_{m,12}^{n+1}), \tag{3.41}$$

$$\mu_{m,12}^{n+1}=H_m^*+\tilde{\beta}(\boldsymbol{\phi}^*)-\epsilon^2\nabla\cdot((1-\phi_0)\nabla\phi_{m,12}^{n+1})+S\phi_{m,12}^{n+1}. \tag{3.42}$$

Eqs. (3.37) and (3.38) are split to be

$$\xi\frac{3\phi_{m,21}^{n+1}}{2\Delta t}+\nabla\cdot(\mathbf{u}^*\phi_m^*)=\frac{1}{Pe}\nabla\cdot((1-\phi_0)\nabla\mu_{m,21}^{n+1}), \tag{3.43}$$

$$\mu_{m,21}^{n+1}=-\epsilon^2\nabla\cdot((1-\phi_0)\nabla\phi_{m,21}^{n+1})+S\phi_{m,21}^{n+1}, \tag{3.44}$$

and

$$\xi\frac{3\phi_{m,22}^{n+1}}{2\Delta t}=\frac{1}{Pe}\nabla\cdot((1-\phi_0)\nabla\mu_{m,22}^{n+1}), \tag{3.45}$$

$$\mu_{m,22}^{n+1}=H_m^*+\tilde{\beta}(\boldsymbol{\phi}^*)-\epsilon^2\nabla\cdot((1-\phi_0)\nabla\phi_{m,22}^{n+1})+S\phi_{m,22}^{n+1}. \tag{3.46}$$

By using the expression of $\hat{R}^{n+1}$, we rewrite Eq. (3.12) to be

$$3\left(\hat{R}_1^{n+1}+\hat{Q}^{n+1}\hat{R}_2^{n+1}\right)-4R^n+R^{n-1}=\frac{1}{2}\int_\Omega\sum_{m=1}^{2}H_m^*\left(3\phi_{m,1}^{n+1}+3\hat{Q}^{n+1}\phi_{m,2}^{n+1}-4\phi_m^n+\phi_m^{n-1}\right)\,d\mathbf{x}. \tag{3.47}$$

Based on the splitting technique, we get

$$3\hat{R}_1^{n+1}-4R^n+R^{n-1}=\frac{1}{2}\int_\Omega\sum_{m=1}^{2}H_m^*\left(3\phi_{m,11}^{n+1}+3\hat{R}_1^{n+1}\phi_{m,12}^{n+1}-4\phi_m^n+\phi_m^{n-1}\right)\,d\mathbf{x}, \tag{3.48}$$

$$3\hat{R}_2^{n+1}=\frac{1}{2}\int_\Omega\sum_{m=1}^{2}H_m^*\left(3\phi_{m,21}^{n+1}+3\hat{R}^{n+1}\phi_{m,22}^{n+1}\right)\,d\mathbf{x}. \tag{3.49}$$

Then, we update $\hat{R}_1^{n+1}$ and $\hat{R}_2^{n+1}$ from

$$\left(3-\frac{3}{2}\int_\Omega\sum_{m=1}^{2}H_m^*\phi_{m,12}^{n+1}\,d\mathbf{x}\right)\hat{R}_1^{n+1}=4R^n-R^{n-1}+\frac{1}{2}\int_\Omega\sum_{m=1}^{2}H_m^*\left(3\phi_{m,11}^{n+1}-4\phi_m^n+\phi_m^{n-1}\right)\,d\mathbf{x}, \tag{3.50}$$

$$\left(3-\frac{3}{2}\int_{\Omega}\sum_{m=1}^{2}H_m^*\phi_{m,22}^{n+1}\,d\mathbf{x}\right)\hat{R}_2^{n+1}=\frac{3}{2}\int_{\Omega}\sum_{m=1}^{2}H_m^*\phi_{m,21}^{n+1}\,d\mathbf{x}. \tag{3.51}$$

To achieve decoupled computation of intermediate velocity, we rewrite Eq. (3.9) as

$$\frac{ReDa}{\xi}\left[\frac{3\tilde{\mathbf{u}}_1^{n+1}+3\hat{Q}^{n+1}\tilde{\mathbf{u}}_2^{n+1}-4\mathbf{u}^n+\mathbf{u}^{n-1}}{2\Delta t}\right]+\alpha(\boldsymbol{\phi}^*)(\tilde{\mathbf{u}}_1^{n+1}+\hat{Q}^{n+1}\tilde{\mathbf{u}}_2^{n+1})=-\nabla p^n-\frac{\hat{Q}^{n+1}\epsilon^{-1}}{We}\sum_{m=1}^{2}\phi_m^*\nabla\mu_m^*$$
$$-\frac{\phi_0}{\kappa}\left(\tilde{\mathbf{u}}_1^{n+1}+\hat{Q}^{n+1}\tilde{\mathbf{u}}_2^{n+1}\right). \tag{3.52}$$

We split it to be

$$\frac{ReDa}{\xi}\frac{3\tilde{\mathbf{u}}_1^{n+1}-4\mathbf{u}^n+\mathbf{u}^{n-1}}{2\Delta t}+\alpha(\boldsymbol{\phi}^*)\tilde{\mathbf{u}}_1^{n+1}=-\nabla p^n-\frac{\phi_0}{\kappa}\tilde{\mathbf{u}}_1^{n+1}. \tag{3.53}$$

and

$$\frac{ReDa}{\xi}\frac{3\tilde{\mathbf{u}}_2^{n+1}}{2\Delta t}+\alpha(\boldsymbol{\phi}^*)\tilde{\mathbf{u}}_2^{n+1}=-\frac{\epsilon^{-1}}{We}\sum_{m=1}^{2}\phi_m^*\nabla\mu_m^*-\frac{\phi_0}{\kappa}\tilde{\mathbf{u}}_2^{n+1}. \tag{3.54}$$

By recasting Eq. (3.13), we have

$$3\hat{Q}^{n+1}-4Q^n+Q^{n-1}=2\Delta t\int_{\Omega}\sum_{m=1}^{2}\left[\nabla\cdot(\mathbf{u}^*\phi_m^*)(\mu_{m,1}^{n+1}+\hat{Q}^{n+1}\mu_{m,2}^{n+1})\right]$$
$$+\sum_{m=1}^{2}\left[\phi_m^*\nabla\mu_m^*\cdot(\tilde{\mathbf{u}}_1^{n+1}+\hat{Q}^{n+1}\tilde{\mathbf{u}}_2^{n+1})\right]\,d\mathbf{x}. \tag{3.55}$$

We update $\hat{Q}^{n+1}$ from the following equality

$$\left(3-2\Delta t\int_{\Omega}\sum_{m=1}^{2}\left[\nabla\cdot(\mathbf{u}^*\phi_m^*)\mu_{m,2}^{n+1}\right]+\sum_{m=1}^{2}\left[\phi_m^*\nabla\mu_m^*\cdot\tilde{\mathbf{u}}_2^{n+1}\right]\,d\mathbf{x}\right)\hat{Q}^{n+1}=4Q^n-Q^{n-1}$$
$$+2\Delta t\int_{\Omega}\sum_{m=1}^{2}\left[\nabla\cdot(\mathbf{u}\phi_m^*)\mu_{m,1}^{n+1}\right]+\sum_{m=1}^{2}\left[\phi_m^*\nabla\mu_m^*\cdot\tilde{\mathbf{u}}_1^{n+1}\right]\,d\mathbf{x}. \tag{3.56}$$

With computed $\hat{Q}^{n+1}$, ϕ_m^{n+1}, μ_m^{n+1}, and $\tilde{\mathbf{u}}^{n+1}$ can be explicitly obtained via back substitution. In each time step, we only need to solve several linear elliptic type equations in a totally decoupled manner.

4. Numerical experiments

In this section, extensive numerical simulations will be performed to validate the stability, accuracy, and capability of our proposed model and algorithm. The governing equations are discretized in space based on the finite difference method, see [50,51] and references therein for some details. Unless otherwise requested, we set some parameters as $Re=1$, $We=1$, $Pe=0.1$, $Da=0.05$, $\chi=0.1$, $\xi=0.5$, $\eta_1=\eta_2=1$, $\kappa=1\text{e}{-8}$, $S=2$, $q_1=\frac{0.98}{Pe\xi}$, and $q_2=\frac{1.98We}{\kappa\epsilon^{-1}}$.

4.1. Energy dissipation property and consistency

In this subsection, we first validate the energy dissipation property under different time steps. The full domain is defined as $\Omega=(0,4)\times(0,4)$. A circular solid with radius 1 and center position $(2,1.2)$ is embedded into Ω. The initial droplet with radius 0.7 locates at $(2,2.9)$. The initial velocities and pressure are zero. The left column of Fig. 2 displays the initial state. On $\partial\Omega$, we use periodic boundary condition and homogeneous Neumann boundary condition for scalar variables along x- and y-directions, respectively. The velocities on $\partial\Omega$ are no-slip. In this test, the mesh size is 256×256 and $\epsilon=0.015$. Let $h=4/256=1/64$ be the space step, we perform the simulations with different time steps: $\Delta t=h(4\delta t)$, $0.5h(2\Delta t)$, and $0.25h(\delta t)$. The evolutional processes of liquid interface with

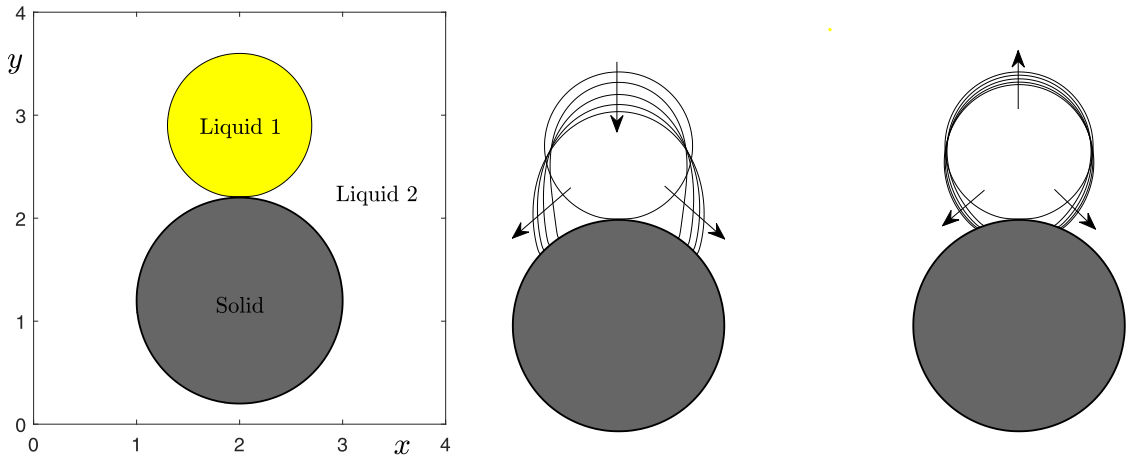

Fig. 2. A droplet locating on a circular solid. (a) initial state; (b) interfacial evolutions with $\theta = 60°$; (c) interfacial evolutions with $\theta = 120°$. The arrows represent the evolutional directions.

Table 1
Exact and numerical results of contact angle θ.

Exact value:	45°	60°	120°	135°
Numerical value:	45.2°	59.7°	119.7°	134.8°

respect to $\theta = 60°$ and $\theta = 120°$ are shown in the middle and the right columns of Fig. 2, respectively. In the left column of Fig. 3, the top and the bottom rows show the interfaces and velocity fields at final stage $t = 25$ with respect to different contact angles. It can be observed that interfacial behavior on the liquid–solid boundary is significantly affected by the contact angle (wetting condition). In the right column of Fig. 3, the curves of original energy and correct energy are plotted. The evolutions are consistent and non-increasing in time. Furthermore, we observe that the energy curve converges as the refinement of time step.

The stabilization parameter S is crucial to obtain stable computation. To test the importance of S, we let $S = 0$ and set a relatively large time step $\Delta t = h$ to perform the same simulations. Fig. 4(a) and (b) display the energy curves with respect to $\theta = 60°$ and $\theta = 120°$, respectively. We observe that the energy dissipation law is not satisfied. As shown in Fig. 3, $S = 2$ leads to energy dissipation-preserving results. It is worth noting that the theory of an optimal stabilization parameter in SAV type method is still an open question. As reported in [48,49] and the references therein, S is an empirical parameter and a relatively small value of S maintaining the energy stability should be used because a large value of S introduces extra errors. Therefore, $S = 2$ will be an appropriate choice in the present work.

If we consider the evolution of a droplet on a flat substrate, the contact angle boundary condition can be explicitly imposed on the boundary of computational domain, see [52–55] and the references therein. As we have mentioned in the Introduction, this treatment requires us to artificially define appropriate boundary conditions. On the contrary, our proposed model do not need explicit boundary conditions and the contact angle can be implicitly achieved after the evolution of governing equations. To verify this, we simulate the evolution of a droplet located on a flat substrate ($y < 0.15$). The full computational domain is $\Omega = (0, 4) \times (0, 2)$. The droplet with radius 0.8 locates at $(2, 0.15)$. Here, we use $\Delta t = 0.25h$ and $h = 1/64$. Fig. 5 shows the initial condition. In Figs. 6 and 7, we display the interfacial evolutions and final stages with respect to $\theta = 45°$, $60°$, $120°$, and $135°$. The droplet presents a hydrophilic property as the presupposed angle is less than 90°. Otherwise, the hydrophobic phenomenon is observed when we let $\theta > 90°$. The exact and numerical values of contact angle are list in Table 1, it can be observed that the contact angles are well simulated by the proposed model. Fig. 8(a)–(d) illustrate the energy curves with respect to different contact angles. The results indicate that the original energy and the corrected energy are non-increasing and highly consistent.

To test the effect of correction technique on energy dissipation, we take the droplet locating on a flat substrate with $\theta = 120°$ as an example. In the first case, we set $\Delta t = 0.25h$ and other parameters keep unchanged. Fig. 9(a)

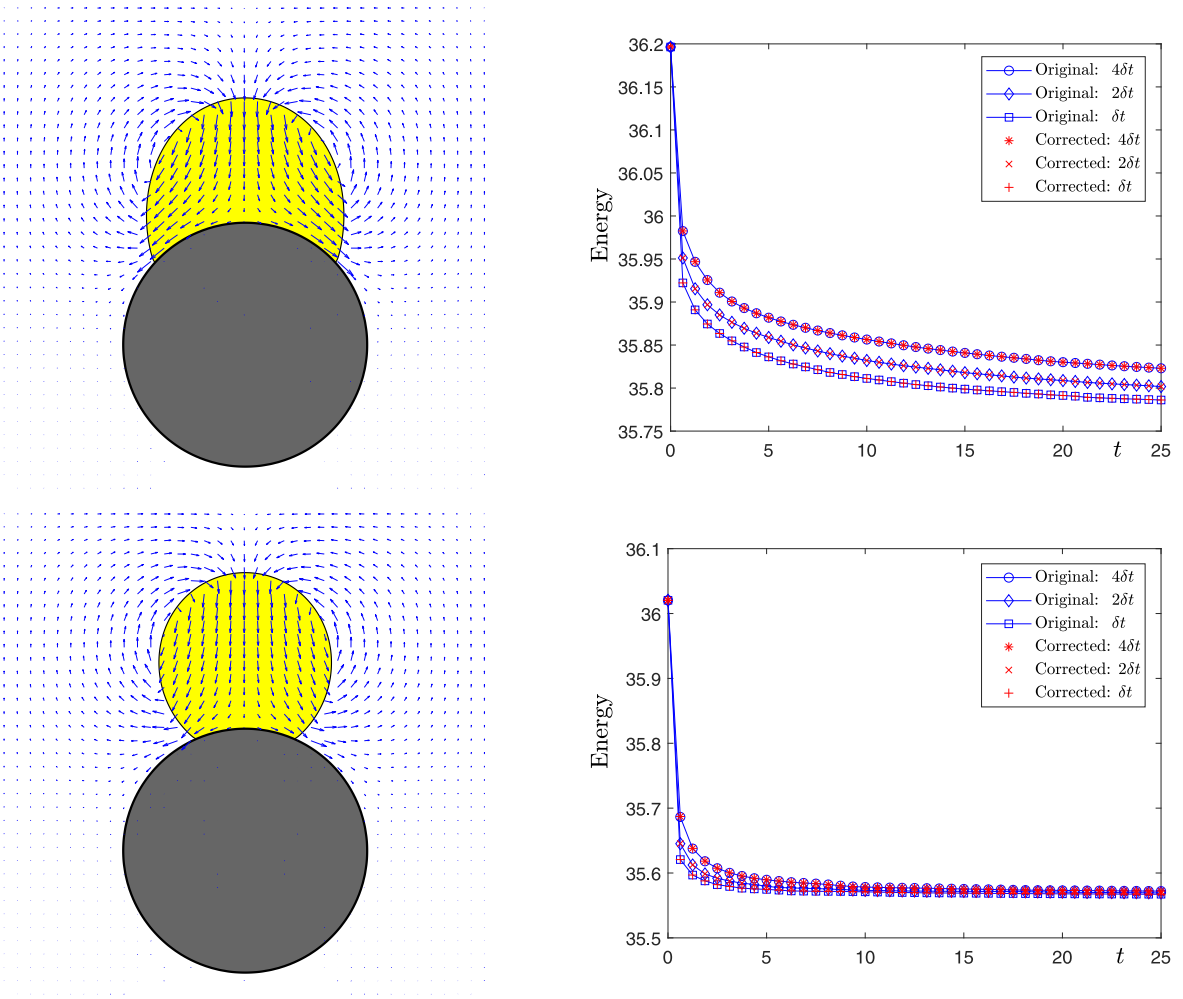

Fig. 3. A droplet locating on a circular solid. The left and right columns show the final stages and energy evolutions. In each column, the top and bottom rows correspond to $\theta = 60°$ and $\theta = 120°$, respectively.

shows the original and modified energy curves without and with energy correction, respectively. From the insets shown in each figure, we observe the difference between original energy and modified energy. Later, we perform the same computations with a larger time step $\Delta t = 2.5h$. From the results in Fig. 9(c), the difference between original energy and modified energy becomes more obvious. On the contrary, Fig. 9(b) and (d) indicate that the correction technique leads to highly consistent results even if a larger time step is used.

To test the consistency between original Darcy model and its numerical form, we perform the same simulation. The left and right columns of Fig. 10 plot the evolutions of Q with respect to $\Delta t = 25h$ and $2.5h$, respectively. With the absence of correction technique on Q, we find that the numerical value of Q obviously deviates from its exact value 1 as the increase of time step. Therefore, the consistency between original Darcy model and the numerical form is destroyed. To perform accuracy simulation, the results indicate that the correction technique on Q is necessary.

For a droplet resting on a flat substrate, we investigate the grid convergence by using mesh sizes: 64×32, 128×64, and 256×128. The initial condition, computational domain, and parameters are unchanged. The contact angle is 120°. The droplet profiles at $t = 15$ with respect to different mesh sizes are plotted in Fig. 11. As we can observe, the droplet profile converges as the refinement of grid.

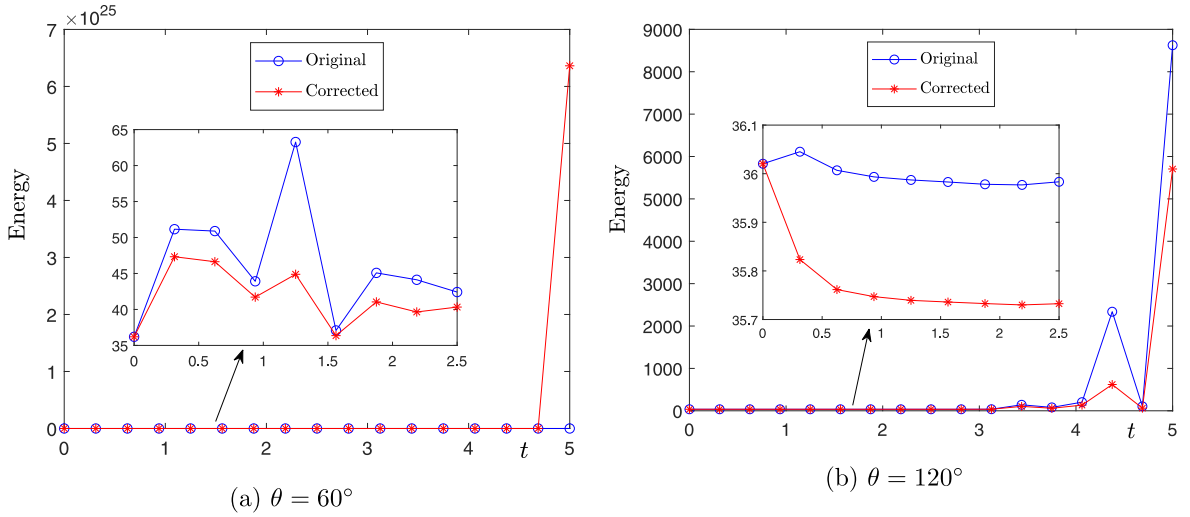

Fig. 4. Energy curves with respect to $S = 0$, (a) $\theta = 60°$, and (b) $\theta = 120°$. The inset in each figure shows the local close-up view of energy curves.

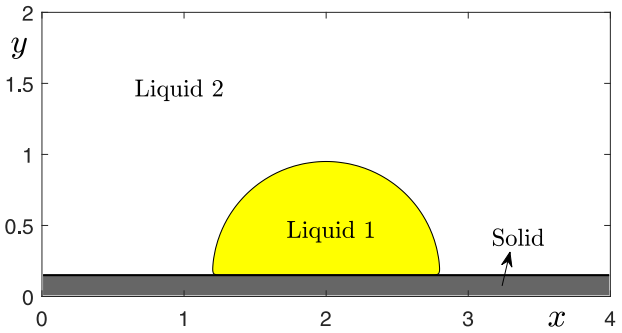

Fig. 5. Initial state of a droplet locating on a flat substrate.

4.2. Effects of different chemical potentials

To derive Eq. (2.5), we neglect the last term in Eq. (2.4) because this term has no contribution on contact angle dynamics. To show the effects of differential chemical potentials: μ_m in Eq. (2.5) and $\tilde{\mu}_m$ in Eq. (2.4), we consider a droplet resting on a flat substrate. The initial radius is 0.8, the initial center position is $(2, 0.15)$. The domain is $\Omega = (0, 4) \times (0, 2)$. We set $h = 1/64$ and $\Delta t = 0.25h$. Fig. 12(a) and (b) show the results at $t = 15$ with respect to $\theta = 60°$ and $120°$, respectively. The numerical results indicate that $\tilde{\mu}_m$ (i.e., the last term in Eq. (2.4)) does not affect the dynamics. Therefore, it is reasonable to neglect this term in Eq. (2.5).

4.3. Comparison with previous method

To simulate the two-phase incompressible fluid flow in contact with solid, Liu and Ding [24] developed a hybrid phase-field immersed boundary method in which the contact angle was imposed based on the geometrical relation. To show the capability of their method, the evolution of a droplet on a cylinder was investigated. By setting the initial area of droplet and the desired contact angle, the analytical profile of droplet can be calculated. Please refer to [24] for some details. In the present simulation, we use the same initial condition on $\Omega = (0, 2.5) \times (0, 2.5)$. The contact angle is $\theta = 30°$. Fig. 13(a) displays the final profiles of droplet obtained by the analytical formula, the previous simulation [24], and the present simulation. The relative errors of droplet area between the present result and the analytical/previous results are listed in Table 2. As we can observe, the relative errors are less than 5%.

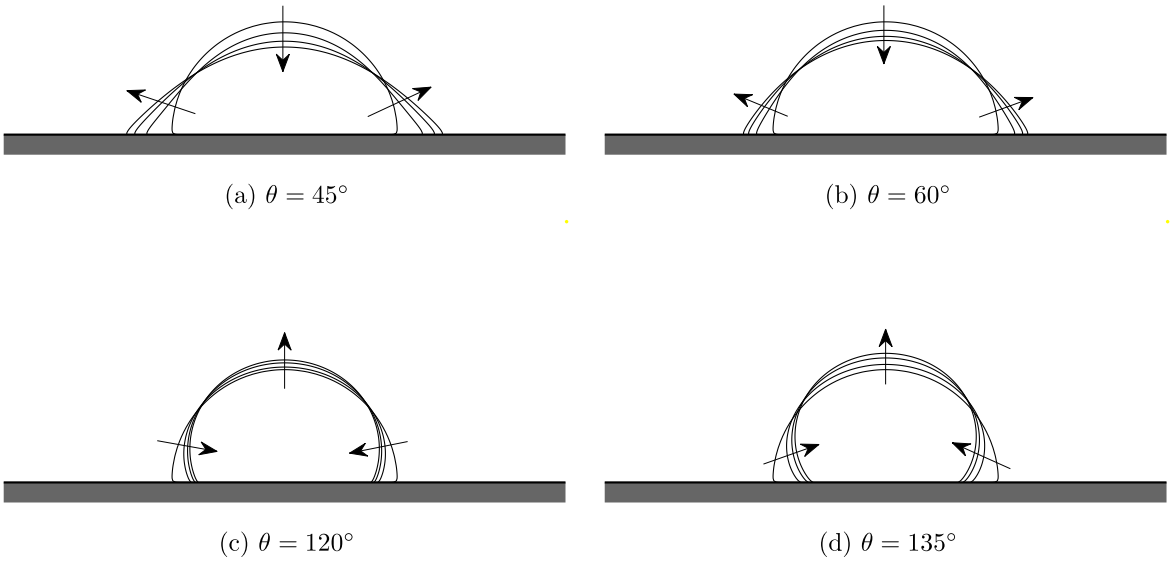

(a) $\theta = 45°$ (b) $\theta = 60°$

(c) $\theta = 120°$ (d) $\theta = 135°$

Fig. 6. Interfacial evolutions of a droplet locating on a flat substrate. Here, the black arrows represent the evolutional directions of liquid interface.

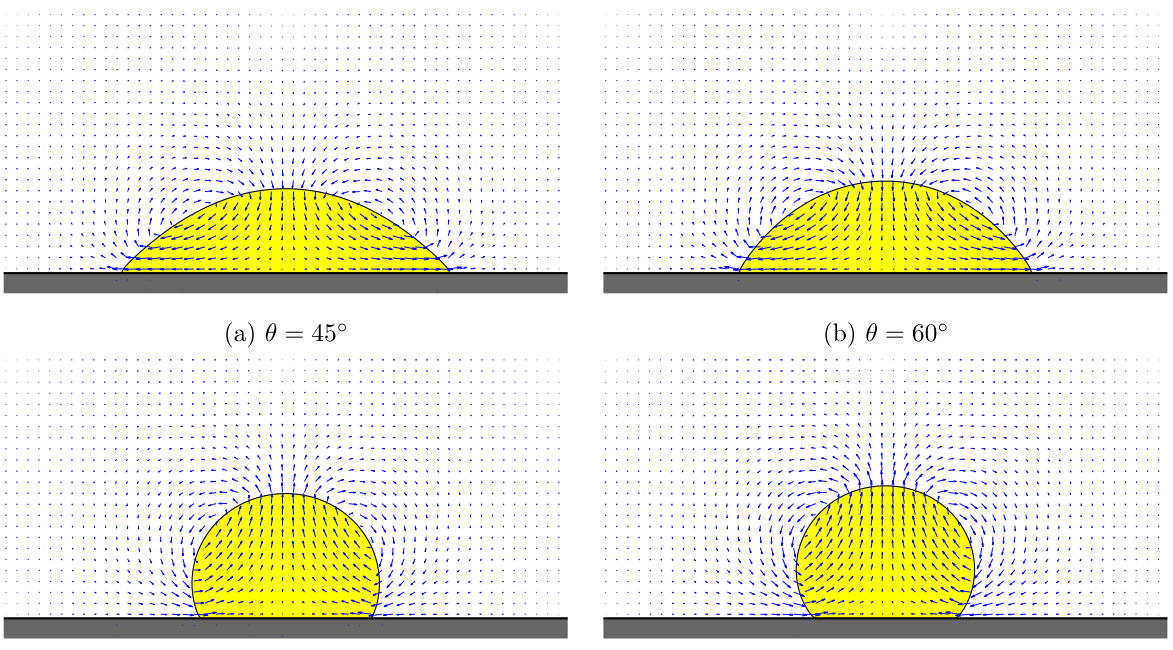

(a) $\theta = 45°$ (b) $\theta = 60°$

(c) $\theta = 120°$ (d) $\theta = 135°$

Fig. 7. Interfaces and velocities of a droplet locating on a flat substrate at final stage $t = 15$. The blue arrows represent the velocity field.

To show the convergence rate, we use the mesh size 256×256 to calculate the reference solution. The time step and ϵ are fixed as $\Delta t = 3.8\text{e}{-4}$ and $\epsilon = 0.0657$, respectively. The L^2-errors corresponding to different mesh sizes: 128×128, 64×64, 32×32, and 16×16 are plotted in Fig. 13(b). The results indicate that our method has second-order accuracy in space.

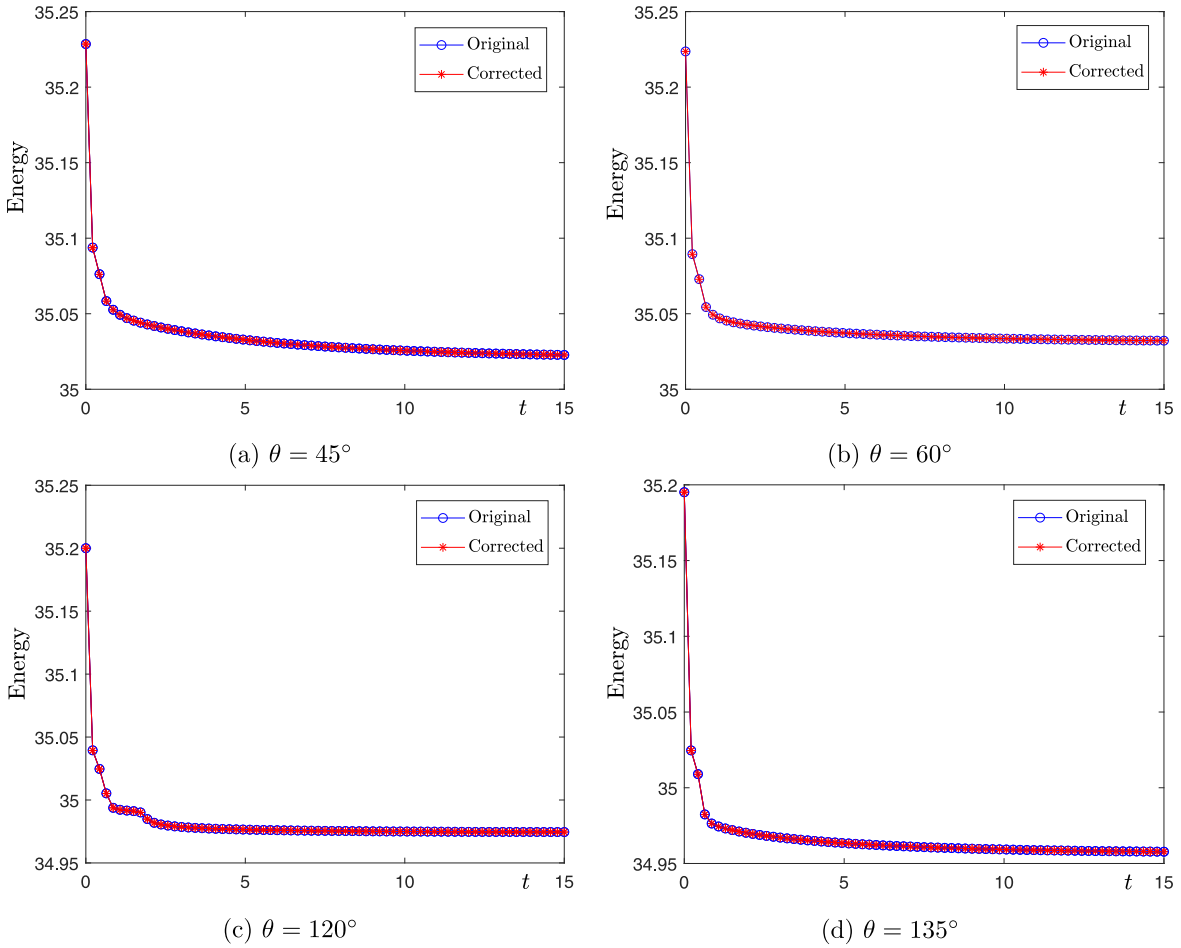

Fig. 8. Energy dissipations of a droplet locating on a flat substrate. The original and corrected values are highly consistent.

Table 2
Areas of droplet and relative errors.

	Analytical	Previous [24]	Present
Area:	0.6547	0.6520	0.6236
Relative error:	4.75%	4.36%	

4.4. Accuracy test

To test the temporal accuracy of our proposed time-marching scheme, we consider a specific case (i.e., a droplet located on a flat substrate with $\theta = 120°$). The reference solutions are obtained by using a small time step $\Delta t^{\mathrm{r}} = 0.025h^2$, where $h = 1/64$ is the space step. The computations are performed by setting increasingly coarser time steps: $\Delta t = 4\Delta t^{\mathrm{r}}$, $8\Delta t^{\mathrm{r}}$, and $16\Delta t^{\mathrm{r}}$. The log–log views of L^2-errors for ϕ_m $(m = 1, 2)$ and velocities (u, v) are plotted in Fig. 14(a) and (b), respectively. The numerical results indicate that the proposed scheme has the temporal accuracy which is not less than second-order.

4.5. Creeping flow coupled phase separation

The binary phase separation is a typical benchmark problem for the CH dynamics. In this subsection, we investigate the creeping flow-coupled phase separation in various irregular domains. In 2D space, the full domain

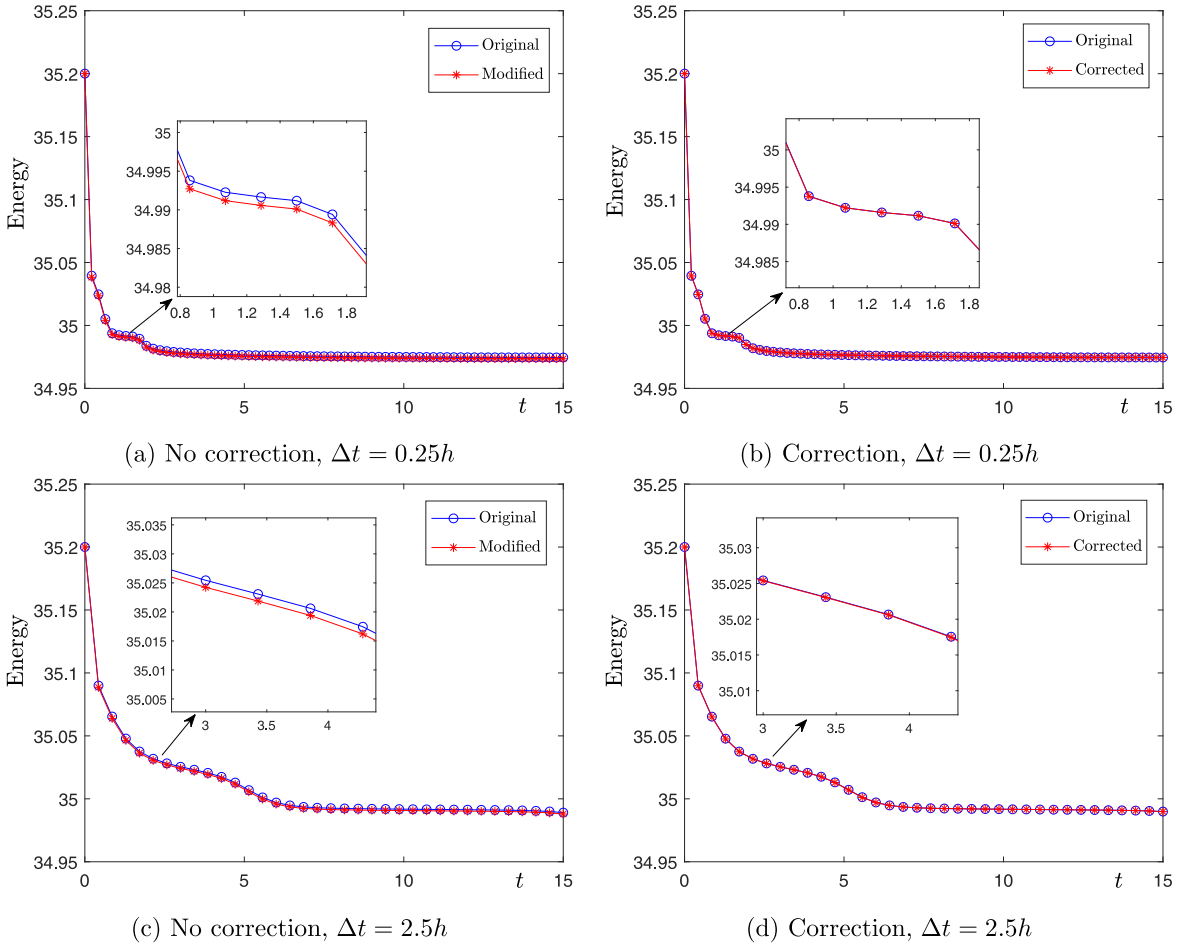

Fig. 9. Effect of correction technique on the evolutions of energy curves. The top and bottom rows show the results with respect to different time steps.

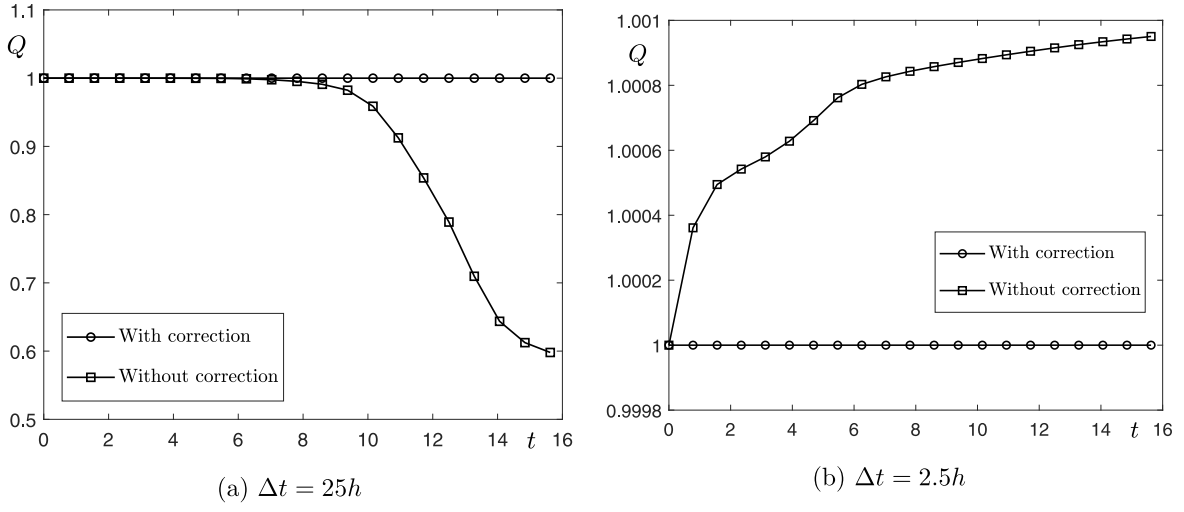

Fig. 10. Effect of correction technique on Q. The left and right columns show the results with respect to different time steps.

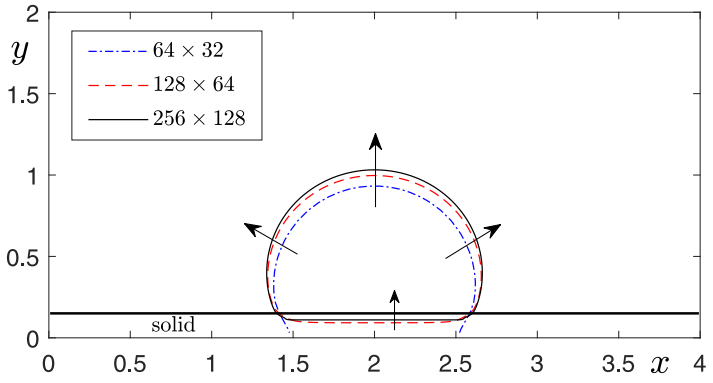

Fig. 11. Droplet profiles with respect to different mesh sizes. Here, the arrows represent the convergence directions.

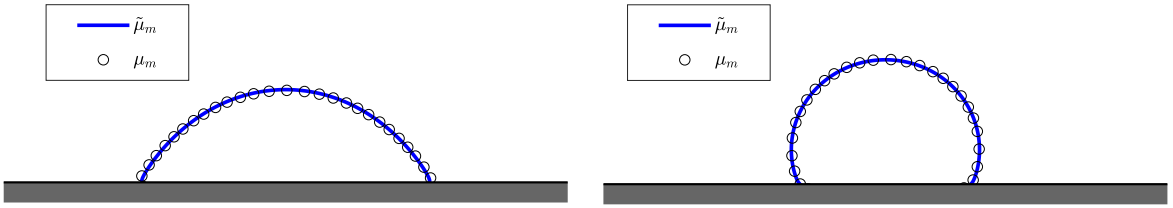

Fig. 12. Effects of μ_m and $\tilde{\mu}_m$ on the droplet spreading. Here, (a) and (b) correspond to $\theta = 60°$ and $120°$.

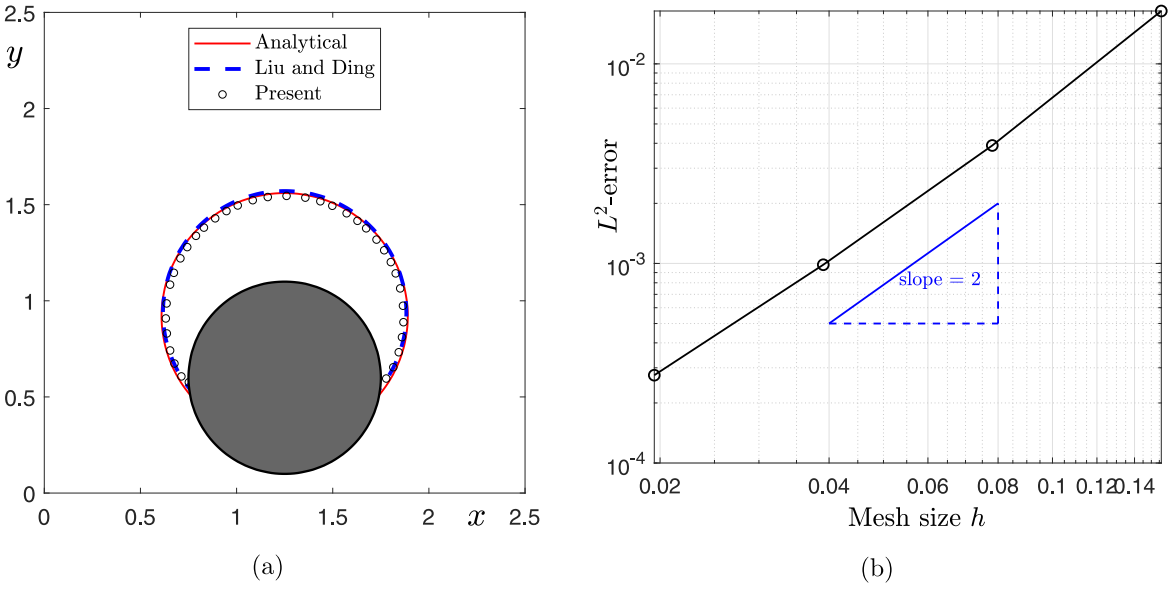

Fig. 13. (a) Profiles of droplet with respect to analytical formula, previous simulation (Liu and Ding [24]), and present simulation. (b) L^2-errors with respect to different mesh sizes.

is $\Omega = (0, 4) \times (0, 2)$. The complex tube is defined by the following two functions

$$y_1 = 0.01x^2 \cos(4\pi x) - 0.04 \sin(8\pi x) + 0.5,$$
$$y_2 = 0.06\sqrt{(2x)} \sin(4\pi x) + 1.3.$$

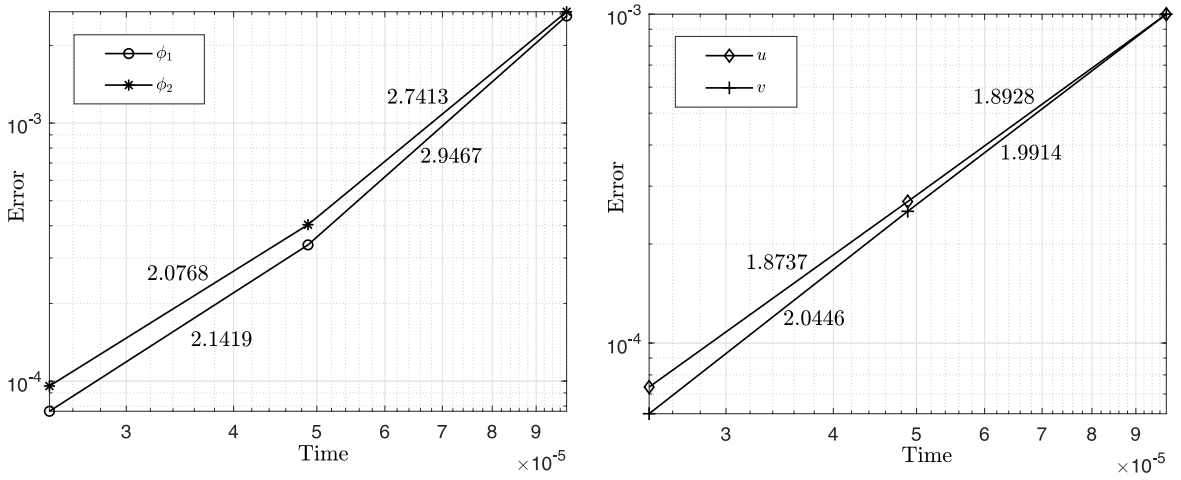

Fig. 14. Accuracy test for (a) ϕ_m $(m = 1, 2)$ and (b) velocities. In each figure, the convergence rates are shown.

The initial conditions of ϕ_1 and ϕ_2 are the sets of random numbers with an average concentration 0.7 and perturbation 0.1. The initial velocities and pressure are zero. On $\partial\Omega$, we consider the homogeneous Neumann boundary condition. We set $\Delta t = 0.001$, $h = 1/64$, $\theta = 90°$, and $\epsilon = 0.0075$. Fig. 15 shows the snapshots of creeping flow-coupled binary phase separation in a 2D irregular tube. The evolution of velocity field is accompanied by the coarsening process. The energy dissipation properties are displayed in the bottom row of Fig. 15.

In 3D space, the full domain is $\Omega = (0, 2)\times(0, 1)\times(0, 1)$. The irregular tube is defined by the following function

$$\phi_0(x, y, z, 0) = 0.5 + 0.5\tanh\left(\frac{\sqrt{(y-0.5)^2+(z-0.5)^2}}{2\sqrt{2}\epsilon} \right.$$
$$\left. \frac{-(0.02x^2\cos(4\pi x) - 0.03\sin(6\pi x) + 0.3)(0.95 - 0.4\cos(\vartheta + \pi x))}{2\sqrt{2}\epsilon}\right), \tag{4.1}$$

where $\vartheta = \tan^{-1}(y - 0.5, z - 0.5)$ and $z \neq 0.5$. The second irregular domain is the well-known Schwarz P region [56,57], its definition is as follows:

$$\phi_0(x, y, z, 0) = 0.5 + 0.5\tanh\left(\frac{\cos(2\pi x) + \cos(2\pi y) + \cos(2\pi z)}{2\sqrt{2}\epsilon}\right). \tag{4.2}$$

Fig. 16(a) and (b) illustrate the 3D irregular tube and Schwarz P domain, respectively. Figs. 17 and 18 display the snapshots of binary phase separation in irregular tube and Schwarz P, respectively. The numerical results indicate that the flow-coupled coarsening processes can be well simulated in different 3D complex domains. The energy dissipations with respect to two irregular domains are shown in Fig. 19.

In the process of phase separation, the same fluid materials merge with each other to occupy most regions of domain. Due to energy dissipation, the total length of liquid–liquid interface will take its minimum value at final stage. However, the computation up to steady state is very time-consuming. In this subsection, we only display some intermediate results in which the coalescence of same fluid materials can be obviously observed.

4.6. Two-phase buoyancy-driven flow

In a sandwich-shaped liquid system, the light liquid is located at the middle position and the upper and lower regions are occupied by another heavy liquid. Due to the buoyancy force, the heavy liquid falls down and the pinch-off of two-phase interface appears. Lee et al. [32], Han and Wang [33], Yang and Kim [58] numerically

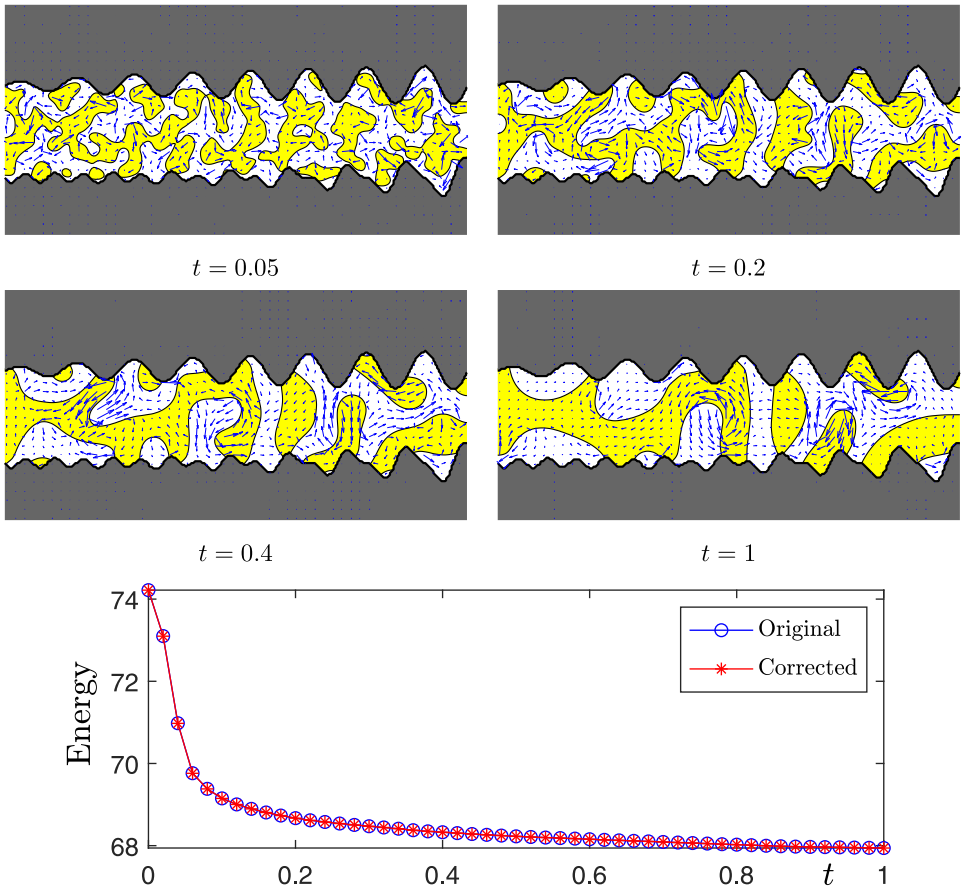

Fig. 15. Creeping flow-coupled binary phase separation in a 2D irregular tube. The liquid–liquid interface is represented by the 0.5-isocontour value of ϕ_1. The solid–liquid interface is represented by the 0.5-isocontour value of ϕ_0. The energy curves are plotted in the bottom row.

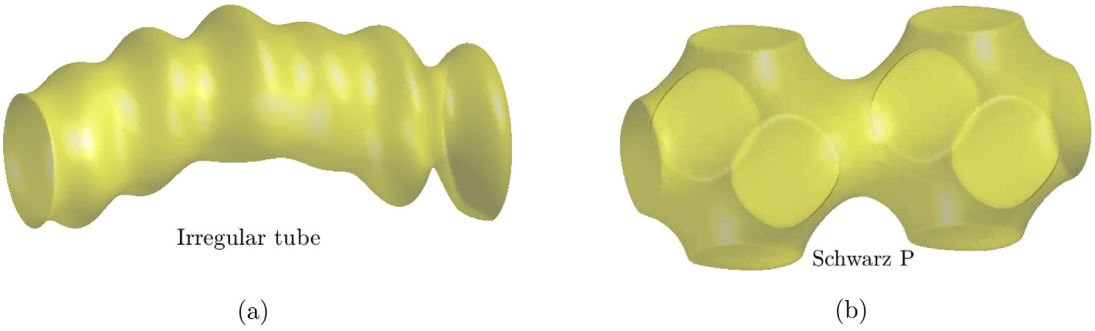

Fig. 16. Schematic illustrations of 3D irregular tube (a) and Schwarz P domain (b). The interface is represented by the 0.5-isocontour value of ϕ_0.

investigated this phenomenon in a regular domain. The Darcy model should be modified to be

$$\frac{ReDa}{\xi}\frac{\partial \mathbf{u}}{\partial t} + \alpha(\boldsymbol{\phi})\mathbf{u} = -\nabla p - \frac{\epsilon^{-1}}{We}\sum_{m=1}^{2}\phi_m \nabla \mu_m + \lambda(\psi - \bar{\psi})\mathbf{g}, \tag{4.3}$$

$$\nabla \cdot \mathbf{u} = 0, \tag{4.4}$$

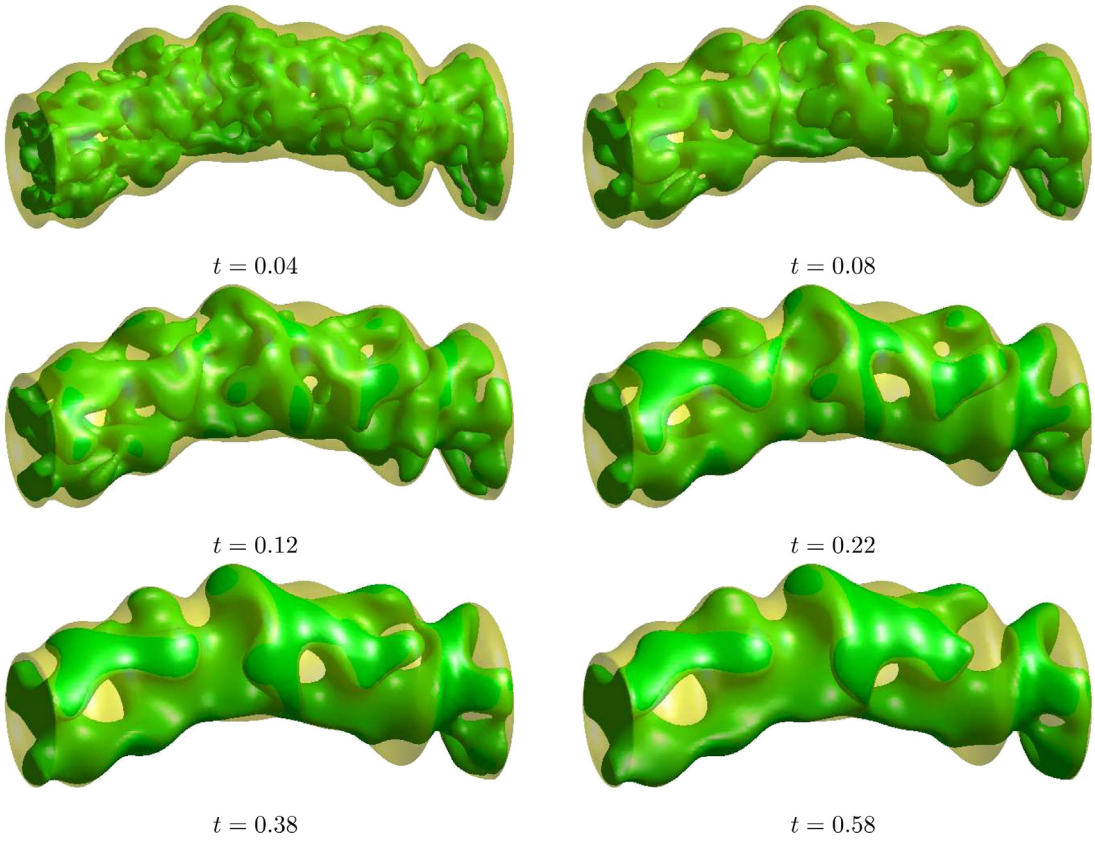

Fig. 17. Creeping-flow coupled binary phase separation in a 3D irregular tube. The computational moments are shown under each figure.

where $\psi = 2\phi_1 - 1$ and $\bar{\psi}$ is the average concentration of ψ, $\mathbf{g} = (0, -g)$ is the gravity. Fig. 20 illustrates the initial state. In this subsection, we aim to simulate the buoyancy-driven creeping flow in contact with a solid. The full domain is $\Omega = (0, 2\pi) \times (0, 2\pi)$. A circular solid with radius 0.5 is located at $(\pi, 0.6\pi + 0.9)$. The initial conditions are defined as

$$\phi_1(x, y, 0) = (1 - \phi_0(x, y)) \left(0.5 + 0.5 \tanh\left(\frac{y - a(x)}{2\sqrt{2}\epsilon}\right) \tanh\left(\frac{y - b(x)}{2\sqrt{2}\epsilon}\right)\right), \tag{4.5}$$

$$\phi_2(x, y, 0) = 1 - \phi_0(x, y) - \phi_1(x, y, 0), \tag{4.6}$$

$$u(x, y, 0) = v(x, y, 0) = p(x, y, 0) = 0, \tag{4.7}$$

where $a(x) = \pi + 0.9 - (0.45 + 0.1\cos(x))$ and $b(x) = \pi + 0.9 + (0.45 + 0.1\cos(x))$. The parameters are set to be $\Delta t = 0.01$, $\epsilon = 0.047$, $Re = 1$, $We = 4$, $Pe = 2$, $Da = 0.035$, $\chi = 0.66$, $g = 1$, and $\lambda = 0.2$. Fig. 21(a) and (b) show the snapshots with respect to $\eta_2 = 10.5$ and $\eta_2 = 1.5$, respectively. In (a) and (b), the contact angle is $\theta = 90°$. We observe that the large viscosity of light liquid obviously delays the evolution. In (c), we set $\eta_2 = 1.5$ and $\theta = 10°$. By comparing the results in (b) and (c), we find that the decrease of θ makes the light liquid adhere to the solid. We also plot the evolutions of Q with respect to three cases in Fig. 22. The results indicate that the numerical value and exact value 1 are highly consistent.

4.7. An extension to ternary liquid system

For the ternary compound droplets in contact with a solid substrate, the interfacial angles: ψ_1, ψ_2, ψ_3 and contact angles: θ_{13}, θ_{12}, θ_{21}, θ_{23} should be considered. A schematic illustration is shown in Fig. 23.

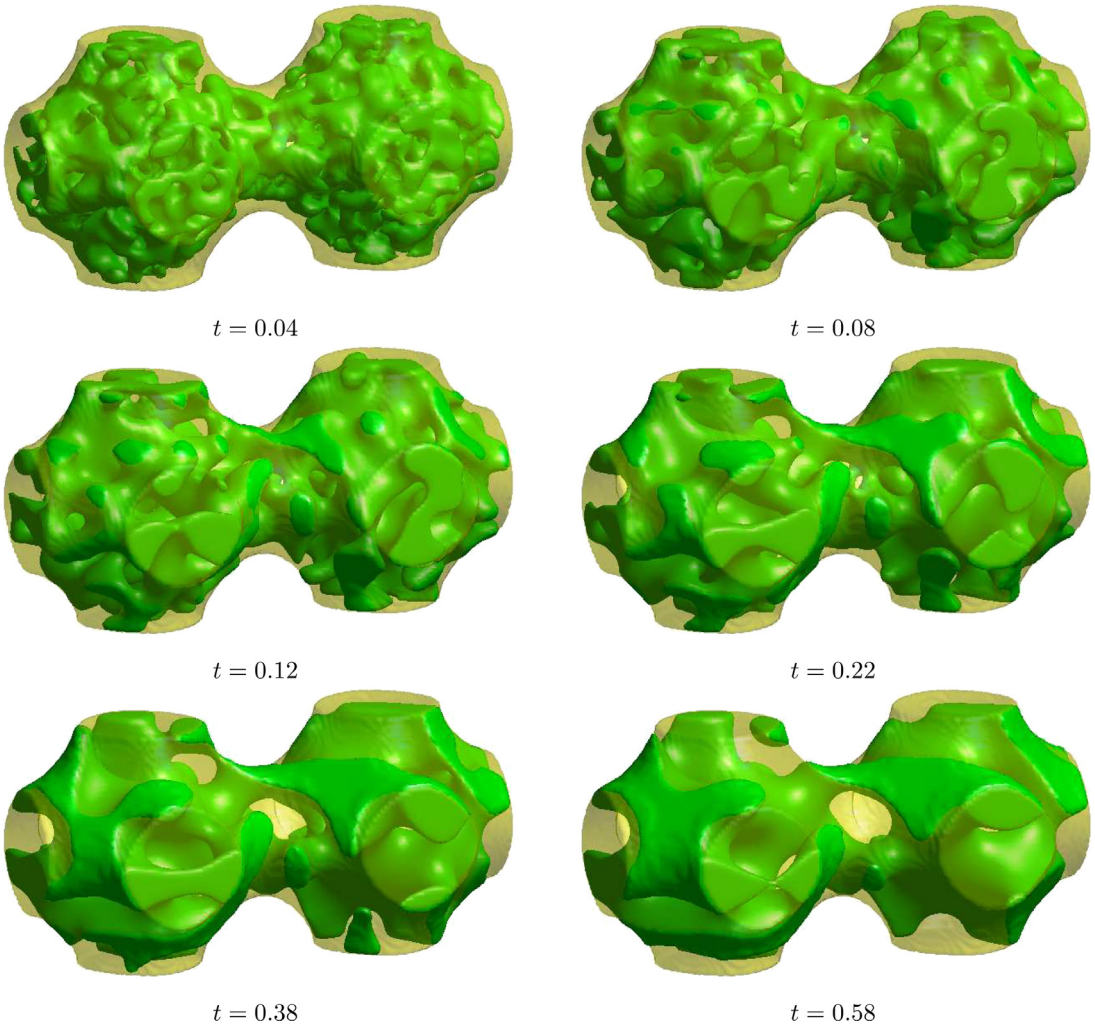

Fig. 18. Creeping-flow coupled binary phase separation in a 3D Schwarz P domain. The computational moments are shown under each figure.

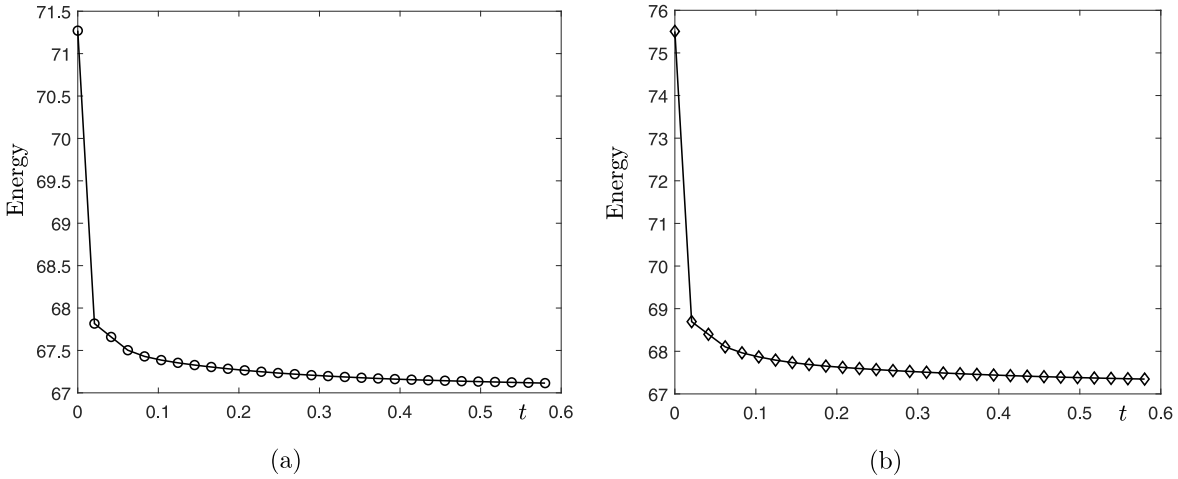

Fig. 19. Evolutions of energy curves with respect to (a) irregular tube and (b) Schwarz P.

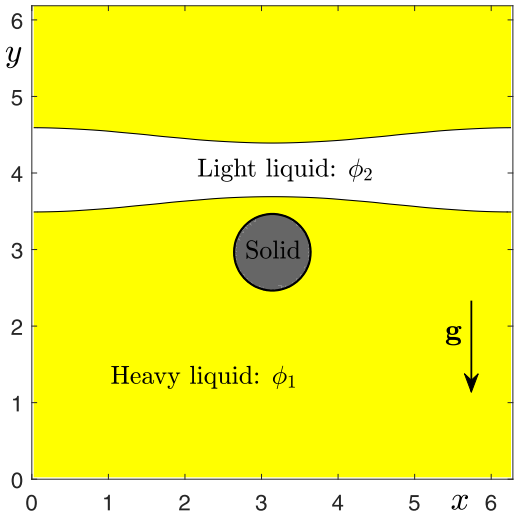

Fig. 20. Initial state of the buoyancy-driven creeping flow.

The balance relation between interfacial angles and surface tensions on liquid interfaces are

$$\frac{\sin\psi_1}{\sigma_{23}} = \frac{\sin\psi_2}{\sigma_{13}} = \frac{\sin\psi_3}{\sigma_{12}}. \tag{4.8}$$

On the boundary between liquid and solid, the Young's equality reads as

$$\sigma_{pq}\cos\theta_{pq} = \sigma_{pS} - \sigma_{qS}, \tag{4.9}$$

where p and q are $1, 2, 3$ and $p \neq q$. In [54], authors derived the following force balance relation from Eqs. (4.8) and (4.9)

$$\sin\psi_2\cos\theta_{13} - \sin\psi_3\cos\theta_{12} - \sin\psi_1\cos\theta_{23} = 0. \tag{4.10}$$

The aforementioned equality indicates that the contact angles and interfacial angles are linked with each other. With known interfacial angles and two presupposed contact angles, the wetting state of compound droplets is well-determined. To simulate the compound droplets in contact with solid in our proposed framework, we herein define three weighted angles as follows:

$$\theta_1 = \frac{\phi_3}{\phi_2+\phi_3}\theta_{13} + \frac{\phi_2}{\phi_2+\phi_3}\theta_{12}, \tag{4.11}$$

$$\theta_2 = \frac{\phi_3}{\phi_1+\phi_3}\theta_{23} + \frac{\phi_1}{\phi_1+\phi_3}\theta_{21}, \tag{4.12}$$

$$\theta_3 = 180^\circ - \left[\frac{\phi_1}{\phi_1+\phi_2}\theta_1 + \frac{\phi_2}{\phi_1+\phi_2}\theta_2\right]. \tag{4.13}$$

We successively choose θ_1, θ_2, and θ_3 when we update ϕ_1, ϕ_2, and ϕ_3, respectively. It is worth noting that this strategy allows us to directly use the proposed model for a binary liquid system with the absence of explicit treatment of contact angles at different positions. In this simulation, the full domain is defined as $\Omega = (0, 4) \times (0, 2)$. A generalized continuous surface tension model [37] for N-component fluid system ($N \geq 3$) is adopted. Fig. 24(a) shows the initial state of compound droplets with radius 1 in contact with a tilted substrate. The parameters are $\Delta t = 0.1$, $h = 1/128$, $\epsilon = 0.0094$, $We = 10/\epsilon$, $Re = 1$. The interfacial angles are 120°, we set $\theta_{23} = 90^\circ$ and $\theta_{23} = 60^\circ$. From the balance relation, $\theta_{12} = 120^\circ$ is obtained. The initial velocities and pressure are set to be zero. The interfacial evolutions and final state ($t = 180$) are shown in Fig. 24(b) and (c), respectively. The numerical values of contact angles are $\theta_{13} = 89.4^\circ$, $\theta_{23} = 60.2^\circ$, and $\theta_{12} = 119.1^\circ$. The results indicate that the proposed model also works well in a ternary liquid system with different wetting conditions. It should be noted that the present ternary liquid model with weighted contact angles does not have the energy dissipation law because θ_1, θ_2, and θ_3

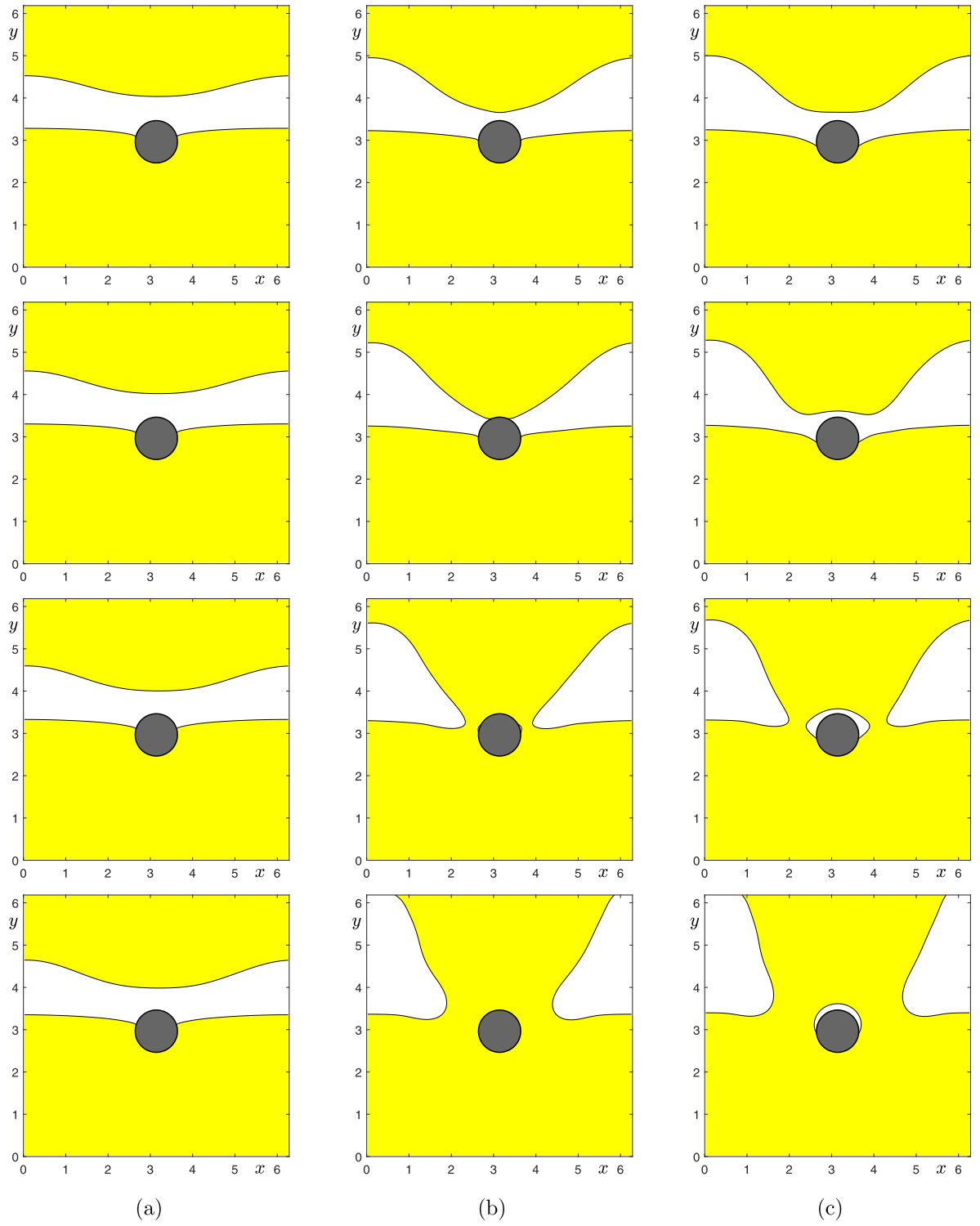

Fig. 21. Buoyancy-driven creeping flow in contact with a solid. Here, (a), (b), and (c) correspond to $(\eta_2, \theta) = (10.5, 90°)$, $(1.5, 90°)$, and $(1.5, 10°)$, respectively. From the top to bottom, the results are at $t = 14$, 16, 18, and 20.

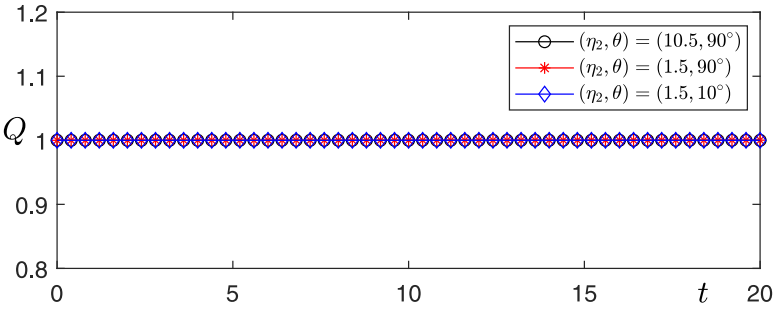

Fig. 22. Evolutions of Q with respect to three cases: $(\eta_2, \theta) = (10.5, 90°)$, $(1.5, 90°)$, and $(1.5, 10°)$.

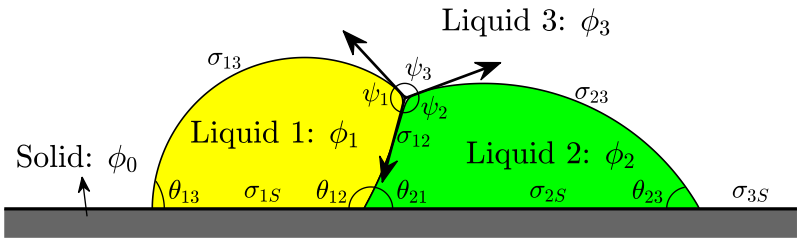

Fig. 23. Schematic illustration of compound droplets in contact with solid substrate.

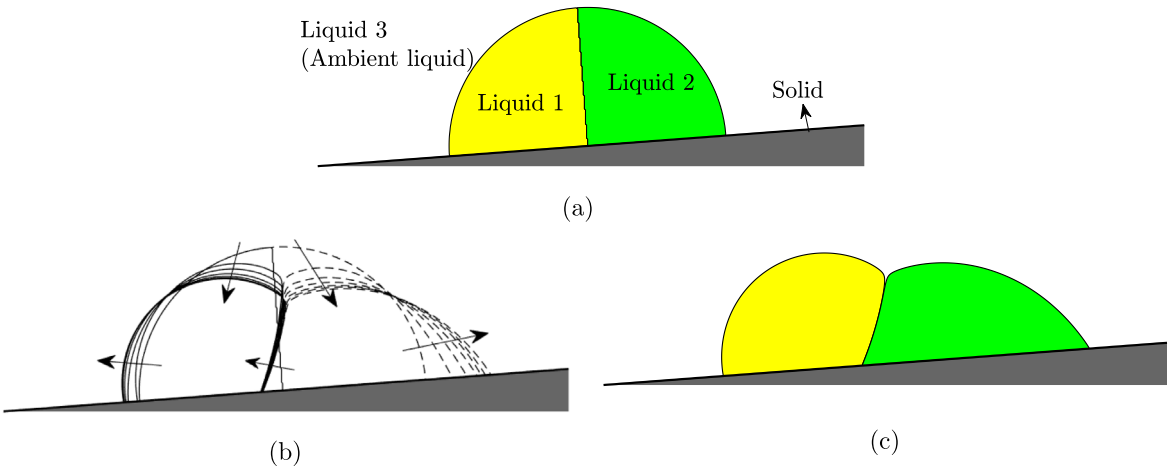

Fig. 24. Compound droplets in contact with a tilted substrate. (a) Initial state; (b) Interfacial evolutions; (c) Final state at $t = 180$. The arrows represent the evolutional directions.

are functions with respect to ϕ_m $(m = 1, 2, 3)$. Moreover, the generalized continuous surface tension model also leads to some difficulties in deriving energy dissipation property. Therefore, we do not consider the energy-stable scheme and only use the BDF2 method to update the variables in time. The energy dissipation-preserving ternary model will be further studied in the future. We admit that the imposing of consistent boundary conditions in a ternary CH system will be more challenging than the case presented in this subsection. Since this work mainly focuses on the binary flows in contact with solid, the present test only shows that the proposed model has good potential for a ternary system with simple wetting conditions. In our future works, we will further develop the models for simulating more challenging interaction problems between ternary fluids and solid [59].

Fig. 25 shows the profiles of compound droplets on a tilted substrate with respect to different mesh sizes: 64×32, 128×64, 256×128, and 512×256. The arrows represent the convergence directions. It can be observed that

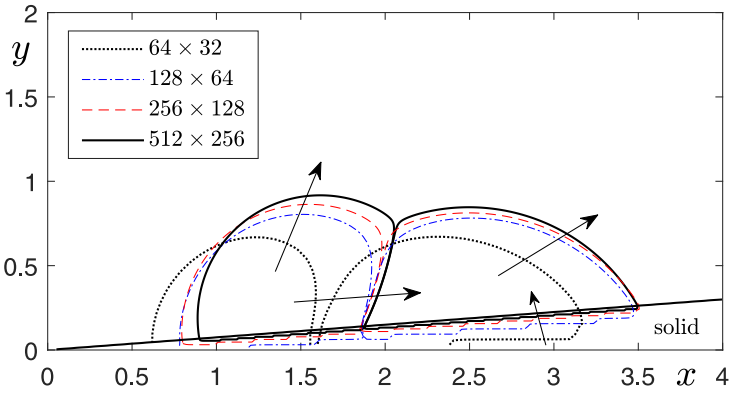

Fig. 25. Profiles of compound droplets with respect to different mesh sizes. Here, the arrows represent the convergence directions.

the numerical result converges as the refinement of grid. The overlap between liquid and solid also vanishes when we refine the mesh.

5. Concluding remarks

This work presented an efficient phase-field fluid model for describing binary creeping flows in contact with solid. A classical ternary CH model was modified to capture the liquid interfaces in irregular domains. The contact angle between liquid phase and solid phase was implicitly achieved by solving the governing equations. The implementation was efficient because the artificial treatment of liquid–solid boundary condition was not necessary. The incompressible Darcy model was modified by adding a penalty term to describe the liquid flows in irregular domains. To satisfy the energy dissipation law of the binary fluid system, we designed a temporally second-order accurate, linearly decoupled, and consistently stable scheme. The discrete energy law was also analytically estimated. The numerical results indicated that the consistent energy stability was satisfied, the arbitrary domains were easily treated, and the contact angle dynamics was well simulated. In our future works, the proposed model and algorithm will be extended to simulate multi-physics coupled fluid systems [60–62] in contact with solid.

Because we only focused on the Darcy type creeping flow in this work, the viscosity was dominant and the Reynolds number in all simulations was low. In a separate work, we will further consider the two-phase fluids governed by the Navier–Stokes equations. By setting a large Reynolds number, the energy evolution in the inviscid limit [63] will be investigated.

Declaration of competing interest

The authors declare that they have no known competing financial interests or personal relationships that could have appeared to influence the work reported in this paper.

Data availability

Data will be made available on request

Acknowledgments

J. Yang is supported by the National Natural Science Foundation of China (No. 12201657), the China Postdoctoral Science Foundation (No. 2022M713639), and the 2022 International Postdoctoral Exchange Fellowship Program (Talent-Introduction Program) (No. YJ20220221). The work of Z. Tan is supported by the National Nature Science Foundation of China (11971502), Guangdong Natural Science Foundation, China (2022A1515010426), Guangdong Province Key Laboratory of Computational Science at the Sun Yat-sen University, China (2020B1212060032), and Key-Area Research and Development Program of Guangdong Province, China (2021B0101190003). The authors thank the reviewers for their constructive comments on this revision.

References

[1] J.-D. Chen, Growth of radial viscous fingers in a Hele–Shaw cell, J. Fluid Mech. 201 (1989) 223–242.
[2] Y. Li, Q. Yu, W. Fang, B. Xia, J. Kim, A stable second-order BDF scheme for the three-dimensional Cahn–Hilliard–Hele–Shaw system, Adv. Comput. Math. 47 (2021) 3.
[3] D. Han, X. Wang, A second order in time, decoupled, unconditionally stable numerical scheme for the Cahn–Hilliard–Darcy system, J. Sci. Comput. 77 (2018) 1210–1233.
[4] Y. Wu, L. Mei, M. Qiu, Y. Chu, A stabilized finite volume element method for stationary Stokes–Darcy equations using the lowest order, Int. J. Comput. Methods 17 (8) (2020) 1950053.
[5] M. Cai, P. Huang, M. Mu, Some multilevel decoupled algorithms for a mixed navier–stokes/darcy model, Adv. Comput. Math. 44 (2018) 115–145.
[6] J. Kim, Phase-field models for multi-component fluid flows, Commun. Comput. Phys. 12 (2012) 613–661.
[7] S.S. Jain, Accurate conservative phase-field method for simulation of two-phase flow, J. Comput. Phys. 469 (2022) 111529.
[8] S.S. Jain, A. Mani, A computational model for transport of immiscible scalars in two-phase flows, J. Comput. Phys. 476 (2023) 111843.
[9] C. Zhang, J. Ouyang, C. Wang, S.M. Wise, Numerical comparison of modified-energy stable SAV-type schemes and classical BDF methods on benchmark problems for the functionalized Cahn–Hilliard equation, J. Comput. Phys. 423 (2020) 109772.
[10] K. Cheng, C. Wang, S.M. Wise, A weakly nonlinear, energy stable scheme for the strongly anisotropic Cahn–Hilliard equation and its convergence analysis, J. Comput. Phys. 405 (2020) 109109.
[11] Y. Qian, C. Wang, S. Zhou, A positive and energy stable numerical scheme for the Poisson–Nernst–Planck–Cahn–Hilliard equations with steric interactions, J. Comput. Phys. 426 (2021) 109908.
[12] R. Mattey, S. Ghosh, A novel sequential method to train physics informed neural networks for Allen Cahn and Cahn Hilliard equations, Comput. Methods Appl. Mech. Engrg. 390 (2022) 114474.
[13] X. Feng, Z. Qiao, S. Sun, X. Wang, An energy-stable Smoothed Particle Hydrodynamics discretization of the Navier–Stokes–Cahn–Hilliard model for incompressible two-phase flows, J. Comput. Phys. 479 (2023) 111997.
[14] Q. Xia, Q. Yu, Y. Li, A second-order accurate, unconditionally energy stable numerical scheme for binary fluid flows on arbitrarily curved surfaces, Comput. Methods Appl. Mech. Engrg. 384 (2021) 113987.
[15] Y. Zhong, H. Fang, Q. Ma, X. Dong, Analysis of droplet stability after ejection from an inkjet nozzle, J. Fluid Mech. 845 (2018) 378–391.
[16] K. Mu, C. Zhang, T. Si, H. Ding, Experimental and numerical investigations on characteristics of coaxial liquid cone in coflow focusing, Phys. Rev. Fluids 7 (2022) 024001.
[17] T.H.B. Demont, G.J. van Zwieten, C. Diddens, E.H. van Brummelen, A robust and accurate adaptive approximation method for a diffuse-interface model of binary-fluid flows, Comput. Methods Appl. Mech. Engrg. 400 (2022) 115563.
[18] A. Bartels, P. Kurzeja, J. Mosler, Cahn–Hilliard phase field theory coupled to mechanics: Fundamentals, numerical implementation and application to topology optimization, Comput. Methods Appl. Mech. Engrg. 383 (2021) 113918.
[19] L. Luo, X.-P. Wang, X.-C. Cai, An efficient finite element method for simulation of droplet spreading on a topologically rough surface, J. Comput. Phys. 349 (2017) 233–252.
[20] Y. Li, J.-I. Choi, J. Kim, Multi-component Cahn–Hilliard system with different boundary conditions in complex domains, J. Comput. Phys. 323 (2016) 1–16.
[21] D. Jeong, J. Yang, J. Kim, A practical and efficient numercial method for the Cahn–Hilliard equation in complex domains, Commun. Nonlinear Sci. Numer. Simul. 73 (2019) 217–228.
[22] J. Kim, Phase field computations for ternary fluid flows, Comput. Methods Appl. Mech. Engrg. 196 (2007) 4779–4788.
[23] Q. Xia, J. Yang, Y. Li, On the conservative phase-field method with the N-component incompressible flows, Phys. Fluids 35 (2023) 012120.
[24] H.-R. Liu, H. Ding, A diffuse-interface immersed-boundary method for two-dimensional simulation of flows with moving contact lines on curved substrates, J. Comput. Phys. 294 (2015) 484–502.
[25] H.-L. Li, H.-R. Liu, H. Ding, A fully 3D simulation of fluid–structure interaction with dynamic wetting and contact angle hysteresis, J. Comput. Phys. 420 (2020) 109709.
[26] J. Shen, J. Xu, J. Yang, The scalar auxiliary variable (SAV) approach for gradient flows, J. Comput. Phys. 353 (2018) 407–416.
[27] M. Sun, X. Xiao, X. Feng, K. Wang, Modeling and numerical simulation of surfactant systems with incompressible fluid flows on surfaces, Comput. Methods Appl. Mech. Engrg. 390 (2022) 114450.
[28] N. Zheng, X. Li, Error analysis of the SAV Fourier-spectral method for the Cahn–Hilliard–Hele–Shaw system, Adv. Comput. Math. 47 (2021) 71.
[29] M. Jiang, Z. Zhang, J. Zhao, Improving the accuracy and consistency of the scalar auxiliary variable (SAV) method with relaxation, J. Comput. Phys. 456 (2022) 110954.
[30] Y. Li, J. Yang, Consistency-enhanced SAV BDF2 time-marching method with relaxation for the incompressible Cahn–Hilliard–Navier–Stokes binary fluid model, Commun. Nonlinear Sci. Numer. Simul. 118 (2023) 107055.
[31] M. Bergmann, J. Hovnanian, A. Iollo, An accurate cartesian method for incompressible flows with moving boundaries, Commun. Comput. Phys. 15 (2014) 1266–1290.
[32] H.G. Lee, J.S. Lowengrub, J. Goodman, Modeling pinchoff and reconnection in a Hele–Shaw cell. I. The models and their calibration, Phys. Fluids 14 (2) (2002) 492–513.
[33] D. Han, X. Wang, Decoupled energy-law preserving numerical schemes for the Cahn–Hilliard–Darcy system, Numer. Methods Partial Differential Equations 32 (3) (2016) 936–954.

[34] F. Boyer, C. Lapuerta, Study of a three component Cahn–Hilliard flow model, Model. Math. Anal. Numer. 40 (2006) 653–687.
[35] J. Zhang, X. Yang, Decoupled, non-iterative, and unconditionally energy stable large time stepping method for the three-phase Cahn–Hilliard phase-field model, J. Comput. Phys. 404 (2020) 109115.
[36] J.-J. Huang, Hybrid lattice-Boltzmann finite difference simulation of ternary fluids near immersed solid objects of general shapes, Phys. Fluids 33 (2021) 072105.
[37] J. Kim, A generalized continuous surface tension force formulation for phase-field models for immiscible multi-component fluid flows, Comput. Methods Appl. Mech. Engrg. 198 (2009) 3105–3112.
[38] S. Dong, Multiphase flows of N immiscible incompressible fluids: A reduction-consistent and thermodynamically-consistent formulation and associated algorithm, J. Comput. Phys. 361 (2018) 1–49.
[39] J.M. Park, P.D. Anderson, A ternary model for double-emulsion formation in a capillary microfluidic device, Lab Chip 12 (2012) 2672–2677.
[40] K. Mu, H. Ding, T. Si, Experimental and numerical investigations on interface coupling of coaxial liquid jets in co-flow focusing, Phys. Fluids 32 (2020) 042103.
[41] A.A. Howard, A.M. Tartakovsky, A conservative level set method for N-phase flows with a free-energy-based surface tension model, J. Comput. Phys. 426 (2021) 109955.
[42] Q. Xia, J. Yang, Y. Li, On the conservative phase-field method with the N-component incompressible flows, Phys. Fluids 35 (2023) 012120.
[43] S. Aland, J. Lowengrub, A. Voigt, Two-phase flow in complex geometries: A diffuse domain approach, Comput. Model. Eng. Sci. 57 (1) (2010) 77–106.
[44] Z. Guo, F. Yu, P. Lin, S. Wise, J. Lowengrub, A diffuse domain method for two-phase flows with large density ratio in complex geometries, J. Fluid Mech. 907 (2021) A38.
[45] J. Kim, A continuous surface tension force formulation for diffuse-interface models, J. Comput. Phys. 204 (2005) 784–804.
[46] H. Liang, X. Hu, X. Huang, J. Xu, Direct numerical simulations of multi-model immiscible Rayleigh–Taylor instability with high Reynolds numbers, Phys. Fluids 31 (2019) 112104.
[47] C.-H. Kim, S.-H. Shin, H.G. Lee, J. Kim, Phase-field model for the pinchoff of liquid-liqudi jets, JKPS 55 (4) (2009) 1451–1460.
[48] X. Yang, A novel fully-decoupled, second-order and energy stable numerical scheme of the conserved Allen–Cahn type flow-coupled binary surfactant model, Comput. Methods Appl. Mech. Engrg. 373 (2021) 113502.
[49] C. Chen, X. Yang, Fully-decoupled, energy stable second-order time-accurate and finite element numerical scheme of the binary immiscible Nematic-Newtonian model, Comput. Methods Appl. Mech. Engrg. 395 (2022) 114963.
[50] G. Zhu, H. Chen, J. Yao, S. Sun, Efficiet energy-stable schemes for the hydrodynamics coupled phase-field model, Appl. Math. Model. 70 (2019) 82–108.
[51] J. Yang, J. Kim, A phase-field method for two-phase fluid flow in arbitrary domains, Comput. Math. Appl. 79 (6) (2020) 1857–1874.
[52] H.G. Lee, J. Kim, Accurate contact angle boundary conditions for the Cahn–Hilliard equations, Comput. & Fluids 44 (2011) 178–186.
[53] H. Ding, P.D.M. Spelt, Wetting condition in diffuse interface simulations of contact line motion, Phys. Rev. E 75 (2007) 046708.
[54] C.-Y. Zhang, H. Ding, P. Gao, Y.-L. Wu, Diffuse interface simulation of ternary fluids in contact with solid, J. Comput. Phys. 309 (2016) 37–51.
[55] G. Zhu, H. Chen, A. Li, S. Sun, J. Yao, Fully discrete energy stable scheme for a phase-field moving contact line model with variable densities and viscosities, Appl. Math. Model. 83 (2020) 614–639.
[56] D. Jeong, J. Yang, J. Kim, A practical and efficient numerical method for the Cahn–Hilliard equation in complex domains, Commun. Nonlinear Sci. Numer. Simul. 73 (2019) 217–228.
[57] Y. Li, Q. Xia, S. Yoon, C. Lee, B. Lu, J. Kim, A simple and efficient volume merging method for triply periodic minimal structure, Comput. Phys. Comm. 264 (2021) 107956.
[58] J. Yang, J. Kim, An efficient stabilized multiple auxiliary variables method for the Cahn–Hilliard–Darcy two-phase flow system, Comput. & Fluids 223 (2021) 104948.
[59] S.R. Bhopalam, J. Bueno, H. Gomez, Elasto-capillary fluid–structure interaction with compound droplets, Comput. Methods Appl. Mech. Engrg. 400 (2022) 115507.
[60] J. Yang, Phase field modeling and computation of multi-component droplet evaporation, Comput. Methods Appl. Mech. Engrg. 401 (2022) 115675.
[61] N. Valizadeh, T. Rabczuk, Isogeometric analysis of hydrodynamics of vesicles using a monolithic phase-field approach, Comput. Methods Appl. Mech. Engrg. 388 (2022) 114191.
[62] X. Pan, K.-H. Kim, J.-I. Choi, Monolithic projection-based method with staggered time discretization for solving non-Oberbeck–Boussinesq natural convection flows, J. Comput. Phys. 463 (2022) 111238.
[63] S.S. Jain, P. Moin, A kinetic energy-and entropy-preserving scheme for compressible two-phase flows, J. Comput. Phys. 464 (2022) 111307.